MICROCOPY RESOLUTION TEST CHART

NATIONAL BUREAU OF STANDARDS-1963-A

LEVEL II

B.S.

A Theory of Anomalous Absorption, Backscatter and Flux Limitation in Laser–Produced Plasmas

D. G. COLOMBANT AND W. M. MANHEIMER

Plasma Theory Branch
Plasma Physics Division

October 11, 1979

DDC
RECEIVED
OCT 23 1979
D

NAVAL RESEARCH LABORATORY
Washington, D.C.

79   10   22   105

SECURITY CLASSIFICATION OF THIS PAGE (When Data Entered)

REPORT DOCUMENTATION PAGE		READ INSTRUCTIONS BEFORE COMPLETING FORM
1. REPORT NUMBER NRL Memorandum Report 4083	2. GOVT ACCESSION NO.	3. RECIPIENT'S CATALOG NUMBER
4. TITLE (and Subtitle) A THEORY OF ANOMALOUS ABSORPTION, BACK-SCATTER AND FLUX LIMITATION IN LASER—PRODUCED PLASMAS.		5. TYPE OF REPORT & PERIOD COVERED Interim report on a continuing NRL problem.
		6. PERFORMING ORG. REPORT NUMBER
7. AUTHOR(s) D. G. Colombant and W. M. Manheimer		8. CONTRACT OR GRANT NUMBER(s)
9. PERFORMING ORGANIZATION NAME AND ADDRESS Naval Research Laboratory Washington, DC 20375		10. PROGRAM ELEMENT, PROJECT, TASK AREA & WORK UNIT NUMBERS NRL Problem 67H02-58A
11. CONTROLLING OFFICE NAME AND ADDRESS U.S. Department of Energy Washington, DC 20545		12. REPORT DATE Oct 1979
		13. NUMBER OF PAGES 67
14. MONITORING AGENCY NAME & ADDRESS(if different from Controlling Office) NRL-MR-4083		15. SECURITY CLASS. (of this report) UNCLASSIFIED
		15a. DECLASSIFICATION/DOWNGRADING SCHEDULE

16. DISTRIBUTION STATEMENT (of this Report)

Approved for public release; distribution unlimited.

17. DISTRIBUTION STATEMENT (of the abstract entered in Block 20, if different from Report)

18. SUPPLEMENTARY NOTES

19. KEY WORDS (Continue on reverse side if necessary and identify by block number)

Laser absorption
Anomalous transport
Stimulated Brillouin backscatter

20. ABSTRACT (Continue on reverse side if necessary and identify by block number)

Fluid simulations of laser light absorption and backscatter are presented for various laser irradiances, wavelengths, target materials, laser pulse lengths and simulated prepulse conditions. Physical processes included in the model are inverse bremsstrahlung, resonant absorption, absorption by ion-acoustic fluctuations, and Brillouin backscatter. For the anomalous processes, self-consistent transport coefficients are derived and used throughout the time-dependent, one-dimensional code. Flux limitation is thus taken into account as a result of the physical processes
(Continues)

DD FORM 1473 EDITION OF 1 NOV 65 IS OBSOLETE
1 JAN 73
S/N 0102-014-6601

i

SECURITY CLASSIFICATION OF THIS PAGE (When Data Entered)

20. Abstract (Continued)

included. Interplay between the various absorption mechanisms and backscatter are uncovered in this study. Comparisons with experiments are presented and suggestions for further experiments are made.

Accession For

NTIS GRA&I ☒
DDC TAB ☐
Unannounced ☐
Justification_____

By_____

Distribution/

Availability Codes

Dist	Avail and/or special
A	

D D C

RECEIVED

OCT 23 1979

D

ii

CONTENTS

iii

I. Introduction

The absorption and backscatter of light in the underdense blowoff of a laser produced plasma, as well as a limitation of electron thermal energy flux all play important roles in laser fusion. This paper constitutes a one dimensional fluid simulation of these and other relevant processes. It is a continuation of our earlier work in this area[1,2] but it models the dynamics of the interaction rather than the steady state. Also included in this work is a study of the effects of Brillouin backscatter. Although our work applies in principle to any laser produced plasma, it is particularly motivated by experiments at the Naval Research Laboratory.[3-6] Experiments there have demonstrated that backscatter through the lens (apparently Brillouin backscatter) can be a very important process for structured laser pulses at sufficiently high intensity.[3-4] Also, more recent experiments with longer pulses[5] (pulse duration of about 3 nsec) have shown very high absorption even at intensities where inverse bremsstrahlung is not effective. For instance at an irradiance of 7×10^{14} W/cm^2, the fractional absorption is about 60%. Also experiments at NRL[6] and elsewhere[7] have shown that absorption is enhanced when the target is in the focal plane of the lens. It has always been our opinion that resonant absorption alone cannot account for all of the absorption.[2] Reference 2 reviews absorption measurements done at many laboratories and comes to this conclusion. The additional mechanism which we propose is ion acoustic turbulence driven by the return current. That mechanism takes place in either an

unmagnetized[1] or magnetized[2] plasma. The fluid simulations reported

here attempt to model this process. A very much oversimplified

picture is that ion acoustic turbulence in the underdense plasma

begins to take over where classical inverse breamsstrahlung becomes

ineffective. For instance, the solid line in Fig. 1 is a schematic

of the total electron-ion momentum exchange collision frequency as a

function of laser irradiance for a Nd laser produced plasma. The

dotted line is a plot of classical inverse bremsstrahlung, while the

dashed line is a plot of the effect of ion acoustic instability.

Roughly speaking, ion acoustic turbulence at high temperature gives

perhaps half as much absorption as inverse bremsstahlung at low

temperature.

One of the principal conclusions of this work is that the absorp-

tion physics falls into two different regimes. In short single

pulse experiments, resonant absorption is the dominant process, but

it gets a strong boost from the ion acoustic turbulence. Typically

the total absorption is about 40% with resonant absorption accounting

for 25% and ion acoustic turbulence for 15%. Most of the light is

specularly reflected, although stimulated Brillouin backscatter plays

a role also. On the other hand, for long pulses or structured pulses,

the physics is usually dominated by a relatively complicated inter-

play between backscatter and ion acoustic turbulence. Both of these

processes depend upon the quasi-linear and nonlinear behavior of a

plasma instability, so the physics is necessarily more speculative

than for instance absorption by inverse bremsstrahlung. This modeling

is more complicated in a fluid simulation but can nevertheless bring

2

a more complete picture of absorption in laser-plasma interactions. Our treatment of these processes is internally self consistent and is based upon well documented theories, simulations and experiments.

We will now briefly contrast our approach to the physics of the underdense plasma with particle simulations and other fluid simulations. Particle simulations have been particularly useful in studying resonant absorption[8-10], strongly driven backscatter instabilities in a laser produced plasma[11] and current driven ion acoustic instabilities in infinite homogeneous plasmas. The problem with the latter two processes is that they are slow compared to the laser frequency so that particle simulations get very expensive. For instance the simulation of Brillouin backscatter in Ref. 11 ran to $t = 7 \times 10^3/\Omega$ (35,000 time steps) with $V_{os}/V_e \sim 7$. However, this is only 3.5 psec for a Nd laser produced plasma, and the total length corresponds to only 10 μm, meaning a density gradient scale length of 1-2 μm. Clearly, a particle simulation for more realistic times, lengths and smaller V_{os}/V_e fields would be astronomically expensive. Our approach sacrifices the detailed description of the instabilities. Its effect is now modeled by anomalous transport in a fluid code. However we gain tremendously in the range of parameters that can be studied. For instance, for a 70 psec Nd laser pulse, we model the entire underdense plasma for the entire pulse duration with . . than two minutes computing time with a TI-ASC.

The other approach, used to study laser-plasma interactions, is fluid simulations (characterized by LASNEX[12-15]). Our simulations have more in common with them than they do with particle simulations

3

but there are still important differences. Specifically our treatment

of flux limitation is quite different. In our model, a large thermal

flux excites an instability. This instability tends to limit the flux,

and gives rise to several other anomalous transport effects. All of

these transport effects can be self consistently related to each other

through the turbulence level. To estimate this level we appeal to

previous experiment, simulation and theory. Thus flux limits are

derived in this work, not specified. Also this work incorporates a

model for Brillouin backscatter. Also, as discussed in the next

section, our approach to electron thermal energy transport is quite

different from that used in LASNEX.[15]

The outline for the remainder of this paper is as follows. In

the next section we discuss the anomalous physical processes in our

simulation models. Section III summarizes the fluid equations which we

solve numerically. Section IV gives results of test runs on the code.

Section V presents a number of different simulations and compares with

experiment. Specifically we look into absorption for short pulses,

long pulses, double structured pulses and absorption as a function of

Z and laser wavelength. Comparisons with recent NRL experiments are

shown. Section VI suggests future experiments and Section VII

summarizes our conclusions.

II. <u>Anomalous Physical Processes</u>

    A. <u>Ion Acoustic Instability Generated by Return Current</u>

        The problem of ion acoustic instability in a plasma which

4

conducts energy has been discussed in a series of papers which deal with both unmagnetized[1,16] and magnetized[2,17] plasmas. In this work we confine our study to unmagnetized plasmas. The basic idea is that if the electrons conduct energy but carry no net current, the flux of energetic particles in the direction of Q (the heat flux) must be balanced by a return current of low velocity particles in the opposite direction. This return current can excite ion acoustic waves which also propagate opposite to Q. There are four principal physical effects of this instability. First of all it reduces the energy flux, or in other words, reduces the electron thermal conduction. Second, it gives rise to an anomalous energy exchange between electrons and ions, with the ions gaining energy and the electrons losing. Third, it gives rises to an electric field which generates the return current (this latter process is not directly calculated in this work because we deal only with the total momentum, not with the momentum of each species separately). These three processes are discussed in detail in Ref. 16. From the quasi-linear theory of a one dimensional spectrum of ion acoustic turbulence which is antiparallel to Q, the calculation of thermal conduction and energy exchange is straightforward and the results are given in the next section.

Fourthly, the ion density fluctuations give rise to enhanced absorption of the laser light.[1,2,16,18] Making a Lorentzian approximation to the electron distribution function, the anomalous collision frequency for absorption of the laser light is from Ref. 16

5

$$\nu_{an} = \frac{\omega_{pe}^2}{\Omega E^2} \, \text{Im} \sum_{\underline{k}} \frac{(\underline{k} \cdot \underline{E})^2}{k^2} \left[\frac{1}{1 + (k\lambda_D)^{-2}} - \frac{1}{1 - \left(\frac{\Omega}{\omega_{pe}} + ik\lambda_D\right)^{-2}} \right] \left| \frac{e\phi(k)}{T_e} \right|^2 \quad (1)$$

where $\underline{E}$ is the electric field of the laser light, Ω is its frequency,
and $\phi(\underline{k})$ is the fluctuating potential due to the ion acoustic wave at
wave number $\underline{k}$. If the laser light incident normal to the plane of the
target and the ion acoustic spectrum is one dimensional, $\underline{k} \cdot \underline{E} = 0$. Of
course the turbulent spectrum is not one dimensional but will exist
within a cone of angle θ with respect to the return current. Since
our results do depend upon $e\phi/T_e$ and θ, it is important to pick these
parameters as accurately as possible. Fortunately we can draw on a
great deal of experimental data[19-26] for, and particle simulations[27-33]
of current driven ion acoustic instabilities. Also there is a great
deal of recent theory[34-38] which examines ion trapping, resonance
broadening or anomalous transport and which basically supports these
data. Our basic assumption is that an ion acoustic instability driven
by a return current will have the same fluctuation level and angular
spread as one driven by a real current.

We will now review some of these data. Mase and Tsukishima[19]
examined a current driven ion acoustic instability and diagnosed it by
microwave scattering. They confirmed that the waves obeyed the linear
dispersion relation and found $\frac{e\phi}{T_e} \sim 0.1$. Also, they measured the
angular spread, about the direction of current, of the wave numbers
of the fully developed turbulence. For $-30^o < \theta < 30^o$, (as far as they
measure in angle) they find a spectrum which is nearly uniform as a

6

function of angle. Finally they confirm that the anomalous electron collision frequency is proportional to $(\frac{e\phi}{T_e})^2$, which supports the quasi-linear theory we invoke.

Also, there are measurements of ion acoustic turbulence in collisionless shocks. The turbulence at $k \lesssim k_D$ itself was first identified by CO_2 laser scattering in the shock front.[20] Later experiments[21] measured the angular width of this spectrum and found $\theta \sim 50^o$ to 60°. A more recent experiment[22] produced ion acoustic turbulence by driving a current through a collisionless plasma column. The linear dispersion relation was verified, and it was found that for a strongly driven system ($V_D \sim 0.15 \, V_e$) the fluctuation level was about 15%. The authors of Ref. 22 also compared the measured collision frequency with that predicted by Choi and Horton.[38] Hamburger[23] also showed that ion acoustic instability could be driven in a toroidal system with high current. However no measurements of fluctuation spectrum or angular spectrum are given. Even in a weakly driven system[24], ion acoustic turbulence can still be excited. In the experiment of Slusher et al[24], the current velocity in He^+ at $T_e = 4eV$ exceeds the threshold velocity by a factor of two or less. Also impurity ions (protons in this case) were found to have a strong stabilizing effect. Nevertheless ion acoustic waves with $k \sim k_D/2$ were observed in accord with linear theory. By CO_2 laser scattering, they found $\frac{e\phi}{T_e} \sim 0.03$ and an angular width of about 30°. Finally, experiments at University of California at Los Angeles also found well diagnosed ion acoustic waves with $k \sim k_D/2$ and which grow to a fluctuation level of $\frac{e\phi}{T_e} \sim 0.1$. These

7

ion acoustic waves could be driven either by an electron current[25] or by the decay of an electron plasma wave.[26]

We now turn to a discussion of particle simulations of current driven ion acoustic turbulence. Lampe et al[27-29] have shown with a one dimensional particle simulation that if a current is perpendicular to an applied weak magnetic field, ion acoustic fluctuations grow as in an unmagnetized plasma. These simulations also confirmed that $k \sim k_D/2$. The instability was found to saturate by ion trapping (see next subsection) with $0.1 < \frac{e\phi}{T_e} < 0.2$. Also these simulations confirmed that the electron dynamics were described by quasi-linear theory.

There are also several simulations of current driven ion acoustic turbulence in two dimensions[30-32]. In Ref. 30, resonant quasi-linear heating was again confirmed for the electrons. Once the system saturated by ion trapping, with $0.1 < \frac{e\phi}{T_e} < 0.2$, the turbulence had a wide angular spectrum, $\theta \sim 55^o - 60^o$. Reference 31 claimed ion trapping is not responsible for saturation. However they see ion acoustic turbulence with $\frac{e\phi}{T_e} \sim 0.1$, $k\lambda_D \lesssim 1$ and a spectrum of angular width $\theta \sim 30^o$. Also they confirm quasi-linear behavior for electrons. Biskamp et al[32] also confirmed that in a two dimensional particle-in-cell simulation, a current drives ion acoustic waves unstable. They found a broad angular spectrum with $\frac{e\phi}{T_e} \gtrsim 0.1$ and $k\lambda_D \lesssim 1$, and the electrons described by quasi-linear theory. Another similar simulation, but in three dimensions[33] confirms these results.

We have modeled the two dimensional nature of the spectrum by assuming that $\phi(k)$ is constant within a cone of angle θ about the

8

direction of the return current, and zero outside. Also we model the
spectrum with a single k. A choice $\theta \approx \pi/3$, $k \sim k_D/2$ and $\frac{e\phi}{T_e} = 0.1$ seems
to be reasonably consistent with the data which we have cited.

Let us finally note that if the plasma is magnetized, the ion
wave has its wave vector perpendicular to both $\underline{B}$ and $\underline{\nabla}T_e$, so k can be
parallel to the electric field over part of the laser spot. Thus not
only can the absorption be enhanced, but also there is no need to make
any assumption concerning angular width of the spectrum. Our study,
which neglects $\underline{B}$, then gives rise to minimum anomalous absorption.

B. Brillouin Backscatter

We now discuss the Brillouin backscatter instability in an
inhomogeneous plasma.[39,40,41] To start, we briefly review the results
of the linear theory of Brillouin backscatter in an inhomogeneous
plasma. Since the flow velocity in the underdense plasma is generally
supersonic, we assume that the group velocity of the reflected wave
and acoustic wave are in the same (outward) direction. However, even
if the group velocities have opposite sign, the result of the theory is
not different.[39,42] In the steady-state, the linear equations for the
incident and reflected wave are

$$V_{gr} \frac{dF_r}{dx} = \gamma_o F_s \exp\left(i \frac{K}{2} x^2\right) \qquad \text{(a)}$$

$$V_{gs} \frac{dF_s}{dx} = \gamma_o F_r \exp\left(-i \frac{K}{2} x^2\right) - \nu_s F_s \qquad \text{(b)}$$

(2)

where F denotes the square root of the action density, a subscript r(s)
denotes the reflected (sound) wave and V_g is the appropriate group

9

velocity. The quantity γ_o is the growth rate for the Brillouin back-scatter instability in the absence of damping of the reflected and sound wave,[40]

$$\gamma_o^2 = \frac{\omega_{pi}^2}{8c} \frac{V_{os}^2}{V_e} \left(\frac{M}{mZ}\right)^{1/2} \tag{3a}$$

where

$$V_{os} = \frac{eE_i}{m\Omega} \quad \text{and} \quad V_e = \left(\frac{T_e}{m}\right)^{1/2} \tag{3b}$$

where E_i is the amplitude of the electric field of the incident laser light. Finally K is the reciprocal of the square of the phase mismatch scale length

$$K \equiv L_{ph}^{-2} = \left|\frac{dk_s}{dx} - \frac{dk_i}{dx} - \frac{dk_r}{dx}\right| = 2k_i \left|\frac{\frac{dv}{dx} + \frac{dC_s}{dx}}{v + C_s} + \frac{1}{2}\frac{d}{dx}\frac{\omega_{pe}^2}{c^2 k_i^2}\right| \tag{3c}$$

where k is the wave vector of the appropriate wave (for Brillouin backscatter $k_r \approx k_i$ and $k_s \approx 2k_i$), and ν_s is the Landau damping rate of the sound wave which will be specified in the next section.

For the case $\nu_s = 0$, the reflected wave travels back towards the laser, and is spatially amplified[39] for

$$|x| < L_c \equiv \gamma_o / K(V_{gs}V_{gr})^{1/2} \tag{4}$$

and the total energy amplification is

$$\exp\left[2\pi\gamma_o^2 / K(V_{gs}V_{gr})^{1/2}\right]. \tag{5}$$

On the other hand, if the sound wave is strongly damped,[40] it is

10

amplified in a region of approximate length

$$|x| < L_c = \frac{\nu_s}{Kv_s} \tag{6}$$

and the total energy amplification is still given by Eq. (5).

Let us now discuss how to model this process in our fluid code. First imagine that the grid size Δx is larger than $2 L_c$. Then a reflected wave, which is in phase here, is amplified only within this particular cell and not in neighboring cells. Thus the cells act independently of each other. If we know the thermal level for the reflected wave, we can figure out how much it is amplified in each cell. This amount is then subtracted from the incident laser light and $2V_s/c$ times this power goes into ion heating[43] (the actual algorithm will appear in the next section). Clearly, if $\Delta x > 2L_c$ the total backscattered light is independent of grid size, since if the grid is twice as large, the thermal level of reflected light in the grid cell is twice as great and so is the total reflection in that grid cell. As an initial reflected noise level, we usually assume that for the grid size chosen, ten energy e-folds in a cell gives total reflection there.

Now we turn to the physics of the more complicated case of $\Delta x < 2L_c$. In this case, the reflected wave amplifies coherently from one cell to the next. To treat this would require keeping track, in each cell, of many different reflected waves which are resonant in many different cells. Because this was not the usual case, we treated the cells as independent of each other. Our approach is to first

11

assume an energy amplification in the cell given by Eq. 5 and then reduce the total amplification by $\Delta x/2L_c$. This gives the right answer if the amplification is coherent for $2L_c/\Delta x$ cells, but of course this algorithm is certainly not as valid as that for the case of $\Delta x > 2L_c$. Actually, our calculations usually show that $\Delta x > 2L_c$.

As we will see, if this linear theory is used, the result is that Brillouin backscatter is an extraordinarily strong process and it dominates the dynamics (that is, the laser light is almost totally reflected) for nearly all gradient scale lengths and incident laser light intensity. Particle simulations have also confirmed that while in the linear regime, Brillouin backscatter can play a dominant role even if the gradient scale length is of order of a free space wavelength.[11] Thus a crucial problem is to see whether any process reduces the strength of Brillouin backscatter instability.

We consider a nonlinear reduction in the growth rate due to ion trapping by the ion acoustic wave. To start, we will show that as the ion wave grows, it is forced into a nonlinear regime. For temporal growth, where $\nu_s = 0$ each photon of incident wave lost produces one photon of reflected light and one phonon of ion acoustic wave. For spatial growth, the situation is different because the group velocity of the photon is much greater than the group velocity of ion acoustic wave.[42,44] Here an incident photon decays into one reflected photon and V_{gr}/V_{gs} reflected phonons. From this, it is a straightforward matter to calculate the saturated value (that is

12

assuming total reflection)

$$\left(\frac{e\phi}{T_e}\right)_{sat} \approx \sqrt{8\frac{n_{cr}}{n}}\left(\frac{V_{os}}{V_e}\right) \tag{7a}$$

where ϕ is the amplitude of the fluctuating potential of the ion
acoustic wave and n_{cr} is the critical density and n is the density at
which the backscatter takes place.

On the other hand, if the ion wave is strongly damped, then
at $x = 0$, Eq. (2b) gives the result

$$\left(\frac{e\phi}{T_e}\right)_{sat} = \frac{\gamma_o}{\nu_s}\sqrt{\frac{V_s}{c}}\left(\frac{2n_{cr}}{n}\right)^{1/2}\frac{V_{os}}{V_e} \tag{7b}$$

where we have assumed that the reflected wave amplitude has the maximum
value, that is, equal to the incident wave.

Now let us get a condition for ion trapping. An ion will
trap if the peak to peak potential energy drop of the acoustic wave is
greater than the difference in energy between the wave phase velocity
and $\sqrt{3}$ times the ion thermal energy (assuming a waterbag distribution
function for the ions[37]). Also, for trapping to have a significant
effect on the ion distribution function, the trapping width must be
larger than the ion thermal speed. Thus we have a double condition
for ion trapping. The value of ϕ for ion trapping is determined by

$$\left(\frac{e\phi}{T_e}\right)_{tr} \gtrsim \begin{cases} \frac{1}{4}\left[1 - \left(\frac{3T_i}{ZT_e}\right)^{1/2}\right]^2 & \text{(a)} \\[4mm] \frac{1}{4}\left(\frac{T_i}{T_e}\right) & \text{(b)} \end{cases} \tag{8}$$

13

where Z is the ion charge. Clearly the saturated value $\left(\frac{e\phi}{T_e}\right)_{sat}$ given in Eq. (7a) is much larger than that required for ion trapping for any reasonable value of V_{os}/V_e. Also, $\left(\frac{e\phi}{T_e}\right)_{sat}$ given by Eq. (7b) is compared to the maximum value of $\left(\frac{e\phi}{T_e}\right)_{tr}$ given by Eq. (8a) and (8b). It is always larger by at least a factor of 5 or 10, and often much more. Therefore, before the photon can be strongly backscattered, the ion acoustic wave is driven into a strongly nonlinear regime.

To describe the backscatter in this regime, we invoke recent theoretical work. [37,45] This work does not utilize an enhanced damping, but rather a modification to the growth rate in the absence of damping. The idea is that there is some power input to the ion acoustic wave. In the linear regime, this power input causes the ion acoustic wave to grow at the proper linear growth rate. However once the ions begin to trap, a small increase in amplitude of the ion acoustic wave traps a few more ions. Since ions abruptly gain a tremendous amount of energy when they are trapped, the power input goes principally into accelerating ions and only slightly into causing wave growth. However the wave does not stop growing completely because the power input is still there. Nevertheless, the growth rate does abruptly drop once ions begin to trap. The calculation of the growth rate is given in Ref. 37 for a wave which grows in time in an homogeneous plasma and in Ref. 45 for a wave which grows in space in an homogeneous but bounded plasma. In either case, it was found that this process could be described in terms of a large reduction, by a factor of between five and ten, of the growth rate γ_o (that is the growth rate if $\nu_s = 0$). We invoke these results. If a comparison of Eqs. (7) and (8) shows that trapping is

14

important, we reduce γ_0 and also L_c, according to Eq. (3c) by this large factor. Depending on whether this new reduced L_c is greater than or less than half a grid cell, we treat this backscatter as incoherent or coherent from cell to cell as discussed previously.

To summarize, we first check to see whether the Brillouin backscatter instability is dominated by ion trapping. Where it is (and it always is in the simulations we have done) we adopt previous theories[37,45] which show that the growth rate γ_0 is substantially reduced. Let us note that the approach used here is very different from that used in Ref. 43. Here we rely on reducing γ_0, and also L_c according to Eq. (4). The latter invokes an increase of L_c (according to Eq. (6)) until it is longer than the plasma size. In a future work, we will give a more detailed discussion of these two approaches.

C. The Problem of Energetic Electrons

Other numerical studies of this problem, principally LASNEX have assumed that the electron energy is transported mostly by energetic electrons which are treated separately. The basic idea is that the classical mean free path is much longer than any characteristic scale length. For instance if T_e = 10keV and $n = 10^{21}$ cm^{-3}, the electron mean free path is roughly one millimeter. Thus a classical fluid model is not valid for these electrons. However separate transport of these electrons is a very complicated procedure and to our knowledge, there is no generally agreed upon procedure for it.

The approach that we adopt is very different. We use a single fluid model and justify it by a large anomalous collision frequency. For instance, if the return current excites an ion acoustic instability

15

with fluctuation amplitude $e\phi/T_e$, the anomalous collision frequency is given roughly by $\omega_{pe}(e\phi/T_e)^2$. Therefore, if $e\phi/T_e \sim 10^{-1}$ the electron mean free path for a 10 keV plasma at $n = 10^{21} cm^{-3}$ is roughly 2 microns. Thus a single fluid approximation is now much more reasonable. Even if the absorption process gives rise to nonthermal electron distributions (for instance resonant absorption almost certainly does[8-11]), if the transport of these energetic electrons is inhibited, a single fluid theory is probably still valid everywhere except right at the position where the nonthermal electrons are accelerated. At these points the thermal temperature we calculate will be some average of the superthermal and thermal temperature actually produced.

Thus our philosophy is to explore the consequences of a single fluid description of the electrons and see where it leads. For one thing we find that the temperature in the underdense plasma is generally much greater than the thermal electron temperature predicted by LASNEX. Our thermal temperature in the underdense region, in fact agrees much better with both the superthermal electron energy of the LASNEX simulations and shown by experiment. Of course there will still be runaway tails on the electron distribution function, but now they perturb rather than dominate the electron transport. We find that this model does give reasonable results. Another great advantage is that it is a very straightforward theory and is very economical to study.

III. Fluid Equations

As mentioned in our earlier work[2], the advantages of a time-dependent approach[46] lie not only in the information it yields on the dynamics of the absorption processes but also in the choice of boundary conditions away from the interaction region (which is itself part of the solution). In the present work, boundary conditions were chosen both in or near the solid and in the underdense region, at densities several orders of magnitude above or below the critical density. The fluid equations given now describe the evolution of mass density, total momentum, electron and ion temperature

$$\frac{\partial n}{\partial t} + \frac{\partial}{\partial x}\ nv = 0 \tag{9}$$

$$\frac{nM}{Z}\frac{\partial v}{\partial t} + \frac{n}{Z}\ Mv\ \frac{\partial v}{\partial x} + \frac{\partial}{\partial x}\left[nT_e + \frac{n}{Z}\ T_i\right] + \frac{\omega_{pe}^2}{16\pi\Omega^2}\frac{\partial}{\partial x}\ (E_i^2 + E_r^2) = 0 \tag{10}$$

$$\frac{\partial}{\partial t}\ \frac{3}{2}\ nT_e + \frac{\partial}{\partial x}\ \frac{3}{2}\ nvT_e + nT_e\ \frac{\partial v}{\partial x} + \frac{\partial Q_e}{\partial x} = c_{Te} + P_{res}$$

$$- P_{brem} + \frac{3m}{M}\ n\nu_c\ (T_i - T_e) + \frac{\nu\ (E_i^2 + E_r^2)}{8\pi}\ \frac{\omega_{pe}^2}{\Omega^2} \tag{11}$$

$$\frac{\partial}{\partial t}\ \frac{3}{2}\ \frac{n}{Z}\ T_i + \frac{\partial}{\partial x}\ \frac{3}{2}\ \frac{n}{Z}\ vT_i + \frac{n}{Z}\ T_i\ \frac{\partial v}{\partial x} + \frac{\partial Q_i}{\partial x} = -c_{Te} + P_{b.s.}$$

$$- \frac{3m}{M}\ n\nu_c\ (T_i - T_e) \tag{12}$$

where n is the electron density, m the electron mass, M the ion mass, v the fluid velocity, T_e and T_i the electron and ion temperature, Z the average ion charge, Q_e and Q_i the electron and ion thermal flux,

17

ν_c and ν the classical and total electron-ion collision frequency ($\nu = \nu_c + \nu_{an}$ where the second subscript stands for anomalous), c_{Te} the anomalous electron-ion energy exchange term, E_i and E_r the incident and reflected laser field intensities, P_{res} the resonant absorption heating power, $P_{b.s.}$ the backscatter heating term. P_{brem} is the bremsstrahlung radiation loss term (at the temperature achieved in the runs, the elements under consideration are completely ionized). The expression for these latter terms are:

$$P_{res} = \alpha E_i^2 \Big|_{x = x_c} \left(1 - \frac{\omega_{pe}^2}{\Omega^2}\right)^{1/2}_{x = x_c} \frac{c}{8 \pi \delta x} \tag{13}$$

$$P_{b.s.} = \frac{v_s}{4\pi} A E_i^2 \left(1 - \frac{\omega_{pe}^2}{\Omega^2}\right)^{1/2} \tag{14}$$

$$P_{brem} = 1.69 \; 10^{-25} \; n^2 Z T_e^{1/2} \tag{15}$$

$$\nu_c = \frac{n \; Z \; \ln \Lambda}{3.5 \; 10^5 \; T_e^{3/2}} \tag{16}$$

where v_s is the ion sound speed and A will be defined later. The parameter α will be discussed also in the next section; x_c is the location of the critical surface. It is important to note that in this model all the absorption processes heat up the electron thermal distribution (because of the fluid modeling). There are no non-thermal tail, nor a double-temperature for the electrons in this work. It has been shown that ion-acoustic turbulence, which is an important part of the absorption physics, does not lead to very flat tail but seems to deposit its energy for electrons with

18

$v \simeq 2\text{-}3V_e$.[16,18,47] Of course this is also true of classical inverse bremsstrahlung.

The electron thermal flux term is defined as:

$$Q_e = - K_T \; n \; \frac{\partial T_e}{\partial x} \tag{17}$$

with

$$K_T^{-1} = K_{an}^{-1} + K_{ce}^{-1} \tag{18}$$

whereas the ion thermal flux term remains classical

$$Q_i = -K_{ci} \; n \; \frac{\partial T_i}{\partial x} \tag{19}$$

The equations for the incident and reflected electric fields read:

$$c \frac{d}{dx} \left(1 - \frac{\omega_{pe}^2}{\Omega^2}\right)^{1/2} E_{i(r)}^2 = - \; (+)\nu \; \frac{\omega_{pe}^2}{\Omega^2} E_{i(r)}^2 - \left(1 - \frac{\omega_{pe}^2}{\Omega^2}\right)^{1/2} A \; E_i^2 \tag{20}$$

where A is the Brillouin backscatter term. It is defined as

$$A = \frac{\exp\left[\frac{2\pi\gamma_o^2 \; L_{ph}^2}{36|V_{gs}V_{gr}|} - 10\right]}{1 + \exp\left[\frac{2\pi\gamma_o^2 \; L_{ph}^2}{36|V_{gs}V_{gr}|} - 10\right]} \; \frac{1}{\text{Max}(\Delta x, L_c)} \tag{21}$$

where Δx is the local grid size, $\gamma_o/6$ the nonlinear spatial growth rate. The factor of 6 models the effect of ion trapping as discussed in the previous section and the factor Max (Δx, L_c) accounts for the fact that L_c (the scattering length) may be longer than a grid cell. In addition to solving Eq. (20), we also solve the equation for the reflected wave with A set equal to zero. This gives the specularly reflected light intensity. Substracting the specularly reflected light from the total reflection gives the Brillouin backscatter.

An important step in the process of solving these equations is the determination of the unstable regions both for the ion-acoustic and Brillouin backscatter instabilities. Unlike the classical terms, the anomalous and backscatter terms are non-zero only when some criteria for these instabilities have been met. We turn now to these criteria and discuss also how they are implemented in the numerical solution.

A. Ion-acoustic Instability

In our steady-state work,[1,2] we solved for the amplitude of the unstable waves and we got the fluctuation density level as part of the solution. Because of the extra physics included in the present work and because of the added constraints due to the time-dependent approach, a simplified treatment for the determination of the effects of the ion-acoustic turbulence was adopted. The level of fluctuation $\frac{e\phi}{T_e}$ was chosen to be a certain prescribed value (0.1 in all the runs except in the test runs reported in the next section). This level $\frac{e\phi}{T_e} \sim 0.1$ is supported by numerous experiments and particle simulations of current driven acoustic turbulence as discussed in the previous section. This fluctuation level enters expressions for the anomalous heat conductivity, the anomalous wave damping collision frequency and the anomalous electron-ion energy exchange term. These quantities are respectively

$$K_{an} = \frac{2\sqrt{2\pi}}{\pi |k|} \quad V_e \quad \left(\frac{e\phi}{T_e}\right)^{-2} \tag{22}$$

20

$$\nu_{an} = \frac{k\lambda_D \left(\frac{\omega_{pe}^5}{\Omega^4}\right)\left(\frac{e\phi}{T_e}\right)^2}{\left[1 - \left(1 + k^2\lambda_D^2\right)\frac{\omega_{pe}^2}{\Omega^2}\right]^2 + 4k^2\lambda_D^2\left(\frac{\omega_{pe}}{\Omega}\right)^2} \left[\frac{\frac{2}{3} - \cos\theta + \frac{1}{3}\cos^3\theta}{1 - \cos\theta}\right] \quad (23)$$

$$C_{Te} = v_s \frac{\pi m}{2\sqrt{2\pi}} \left(\frac{n|k|v_s}{v_e^3} + \frac{1}{4}\frac{(1-\cos 2\theta)}{(1-\cos\theta)}\frac{kQ_e}{v_e^2}\right)\left(\frac{e\phi}{m}\right)^2 \quad (24)$$

where θ is the angle between the unstable ion wave cone and the laser

light direction. It was discussed in the previous section and set to

$\pi/3$ in our calculations. Also k is the average unstable ion wave

vector and taken to be $k_D/2$.

The growth rate of the ion acoustic wave is given by

$$\gamma(k) = \sqrt{\frac{\pi}{8}\frac{m}{M}} \frac{\omega_L^3}{\omega_i^3\left(1 + \frac{6k^2 T_i}{\omega_L^2 M}\right)} \left[\frac{|kQ_e|}{nmV_e^2} - \omega_L\left\{1 + Z\sqrt{\frac{M}{m}}\left(\frac{T_e}{T_i}\right)^{3/2}\right.\right.$$

$$\left.\left.\exp\left(-\frac{\omega_L^2 M}{2k^2 T_i}\right)\right\}\right] \quad (25)$$

with

$$\begin{cases} \omega_L = \frac{\omega_{pi}}{\sqrt{2}}\left\{1 + \left[1 + 12\left(1 + k^2\lambda_D^2\right)\right]^{1/2}\right\}^{1/2} \frac{k\lambda_D}{\left(1 + k^2\lambda_D^2\right)^{1/2}} \\ \omega_i = |k|v_s \end{cases}$$

The procedure for including the anomalous transport coefficients due

to ion-acoustic fluctuations is the following: for every point in

space x, starting with the old value for Q_e (defined at the previous

time step, whether or not it corresponded to an unstable situation),

we calculate γ. We then calculate a new value for Q_e, based on the

21

value obtained for γ. We then recalculate γ to check that its value is consistent with the calculation of Q_e. Iterations are performed until consistency is achieved. We define also a flux limitation factor $f = \dfrac{Q_e}{nmV_e^3}$ which will be shown in the results section. This flux inhibition factor is obtained as part of the solution and as such, is space and time dependent. At low density, f is generally limited by the instability, while at high density the plasma is usually stable with the classical value of f being sufficiently small. Thus the flux limit f is not arbitrarily chosen, but is calculated self consistently. If the f calculated this way is too large, an over-riding flux limit of f = 1.5 is invoked. However, this upper flux limit is almost never used; at most for a few points in space for only the first few time steps of the calculation.

B. <u>Stimulated Brillouin Backscatter Instability</u>

The same type of approach has been adopted for the stimulated Brillouin backscatter instability. The Brillouin backscatter term A is set to zero everywhere at the beginning of each time step and differs from zero only when the following double criterion is met

$$
\begin{cases}
\dfrac{2\pi\gamma_o^2 L_{ph}^2}{36\,|V_{gs}V_{gr}|} > 1 \\[2em]
\gamma_o^2 > \nu_s \nu_r
\end{cases}
\tag{26}
$$

22

where $\nu_{r(s)}$, $V_{gr(s)}$ are the damping rate and group velocity of the reflected (sound) wave

$$\nu_r = \frac{1}{2} \nu \frac{\omega_{pe}^2}{\Omega^2} \tag{27}$$

$$\nu_s = \sqrt{\frac{\pi}{8} \frac{m}{M}} \left(\frac{\omega_L}{\omega_i}\right)^3 \frac{1}{\left(1 + \frac{6k_s^2 T_i}{\omega_L^2 M}\right)} \left[\frac{k_s Q_e}{nm V_e^2} + \omega_L \left\{1 + Z\sqrt{\frac{M}{m}}\left(\frac{T_e}{T_i}\right)^{3/2}\right.\right.$$

$$\left.\left. \exp\left(-\frac{\omega_L^2 M}{2k_s^2 T_i}\right)\right\}\right] \tag{28}$$

with

$$\begin{cases} \omega_L = \frac{\omega_{pi}}{\sqrt{2}} \left\{1 + \left[1 + 12\left(1 + k_s^2\lambda_D^2\right)\frac{T_i}{T_e}\right]^{1/2}\right\}^{1/2} \frac{k_s\lambda_D}{(1 + k_s^2\lambda_D^2)^{1/2}} \\ \omega_i = k_s v_s \end{cases}$$

We have consistently checked that the ion trapping conditions (8a) and (8b) are satisfied. We have also checked that $\nu_s < \omega_L$ so that we expect Eq. (2b) to be valid.

The factor of 10 appearing in Eq. (21) for A was introduced to provide physically a smooth transition between the cases of complete reflection and no reflection at all. It simply means that 10 growth lengths are needed for complete reflection in a cell if the cell size Δx is larger than $2L_c$. Unlike the previous instability, no iteration on time was necessary but we note that γ_o and A depends on the value of the incident field (through V_{os}). The incident field is affected in turn by the Brillouin backscatter. The strong spatial coupling between Brillouin backscatter and the laser light must be

23

reflected in the algorithm and as shown in Appendix A, it was found to be crucial for an acceptable solution to this problem.

IV. Test Runs

In the previous section, the equations were given along with the procedures to calculate various other relevant physical quantities which complete the description of our model. It turns out that three quantities needed to be specified initially; the effects of these quantities on the solution is now investigated. These three quantities are the density fluctuation level $\frac{e\phi}{T_e}$, the fractional absorption due to resonant absorption for any ray reaching the critical density, and the non-linear saturation of the Brillouin backscatter light.

A. Level of Ion Acoustic Density Fluctuations

In our previous steady-state studies[1,2] (unmagnetized and magnetized), we solved for the unstable ion acoustic mode amplitudes and as a result, we obtained calculated values for $\frac{e\phi}{T_e}$. The characteristics of the solution generated were the following: the maximum total fluctuation amplitude reached a level of about 0.1; the fluctuation level maximum spanned a region of a few tens of microns for the unmagnetized case (smaller for the magnetized case but we are not concerned with this case in our study); the same modes made up for most of the total fluctuation level except for some cases where different modes came into play at different locations.

From these results, we took 0.1 as our standard value for the density fluctuation level. In this section only, we varied $e\phi/T_e$ between 0.05 and 0.2. Results have been obtained for a short pulse

24

and a double-structured pulse. These types of initial conditions will be described in detail later. The peak laser irradiance in the former case is 10^{15} W/cm^2 and for the latter is 3×10^{15} W/cm^2. We find that for both cases, the total absorption increases with $\frac{e\phi}{T_e}$ as well as the maximum electron temperature achieved during the course of the run. For the 10^{15} W/cm^2 case, total absorption varies from 31% for $e\phi/T_e = 0.05$ to 63% for $e\phi/T_e = 0.2$ (42% for $e\phi/T_e = 0.1$). The maximum electron temperature ranges from 3.4 keV to 11 keV with 5 keV for the intermediate case. A very similar pattern emerges for the 3×10^{15} W/cm^2 case. The differences are even more accentuated since the total absorption goes from 19% to 69% while the maximum electron temperature varies from 4.8 keV to 19 keV. The conclusions for this test are thus the following:

- The results do depend on the value chosen for the ion acoustic fluctuation level $\frac{e\phi}{T_e}$.

- Because of its dependence on this parameter, this study points out the importance of this absorption mechanism and its definite role in laser light interaction with targets, not only for the enhanced absorption but for the anomalous transport and flux inhibition.

- Because of the dependence of results on $\frac{e\phi}{T_e}$, it is important that this parameter be chosen as accurately as possible. A value $e\phi/T_e \sim 0.1$ is in reasonable agreement with our earlier steady state calculations. Also it is consistent with many simulations, experiments and theories of current driven ion acoustic instability.

B. Fractional Resonant Absorption

Resonant absorption for optimum angle of incidence has been shown[10,11] to be around 50% for p-polarization. Averaging over angles of incidence and over polarizations, a reasonable number for absorption due to this process would be around 20-30%. In the remainder of this work, we have chosen 30% ($\alpha = 0.3$) to be the fraction of the laser light which is absorbed when it reaches the critical density. In this section, we varied α between 0.2 and 0.4. Results have been obtained for the same kind of pulses and initial conditions used for the previous tests. Without going into any detail, the total absorption changes less in these tests than in the previous ones. This is due mainly to the smaller range of parameter variations in this case [factor of 2 variation vs. a factor of 16 variation for $(e\phi/T_e)^2$]. The increase in total absorption follows closely the increase in resonant absorption and in both cases, the backscattering remains almost unchanged. This indicates that for each case, the same regime applies. The increase in maximum electron temperature is very minimal between the 20% and 40% resonant absorption case, of the order of 1 keV. In conclusion, because the range of uncertainty in the resonant absorption level is not as large as for the ion turbulence, the results depend only weakly on the exact level of resonant absorption used in the calculations. For this reason, it is our feeling that its modeling is fairly accurate and that the results shown later properly take into account this absorption mechanism (or any other mechanism occurring near the critical surface).

26

C. Non-linear Saturation of Brillouin Backscatter

In the previous sections, non-linear saturation of the Brillouin backscatter was discussed at length since it constitutes one novelty of this work. In this section, we report on two different kinds of test. First, a run was made for the case of a hydrogen plasma without reduction in growth rate (due to ion trapping) but with the ion heating due to backscatter instability.[43] The initial density gradient scale length was taken to be 10μ (the steeper the gradient is, the less backscatter is expected and observed experimentally) and the laser irradiance was 10^{15}W/cm^2. The backscatter reaches quite high values for this case and is equal to 48% after 70 psec. The total absorption is 18% which is quite low compared to similar runs with similar laser irradiances as will be seen in the results section. Since ion heating gives rise to maximum reduction in growth rate for $Z = 1$, there will be even more backscatter for higher Z (most runs have $Z = 2.6$ corresponding to CH_2 targets in the result section). This test shows clearly the importance of introducing ion trapping in our Brillouin backscatter model. Another series of test involved changing the reduction factor in the linear growth rate in order to mock up the non-linear one. A factor of 6 is commonly used in all production runs. This factor was changed to 5 and 7 in the following runs. For a laser irradiance of 3×10^{15} W/cm^2 and a double-structured pulse (the definition of this term will be given later), the total absorption varied from 28% for the reduction factor of 5 to 58% for the reduction factor of 7. The corresponding backscatter was found to be respectively equal to 55% and 17%. The difference between the 5 and 6 reduction

27

factor cases was quite small. The conclusion for these tests is then that ion trapping is very important in order to simulate results from actual experiments and that the level of backscatter computed is qualitative only.

D. Grid Size

A standard test on grid size (which controls the time step through the Courant-Friedrichs-Levy condition for an explicit scheme) was performed in order to check the validity of the calculations. Besides its numerical significance, this test - where the grid size was halved - is quite important because the physics near the critical density can be quite sensitive to the grid size. For example, it has been pointed out by Rosen et al[14] that they could not see some predictable physical effects near the critical surface because of their too low resolution in that region. Since in most of our calculations, the smallest grid size is just below 2μ near the critical surface, it was quite interesting to see changes - if any - brought by a 1μ cell size in that region. Changes observed were very small, at most of the order of a percent or so on most quantities. This is in fact what was expected because the Nd laser light wavelength is 1μ in vacuum only, and increases near cut-off due to WKB enhancement. Features due to the ponderomotive force like the lower density shelf as reported in other works[10,11,48] was well observed as well as the upper density shelf in some cases. Emphasis will not be placed on these features in the next section since this is not the main subject of our study.

28

V. Production Runs

Runs were made for various laser pulse intensities, for various
initial density gradients, for various elements and for several laser
wavelengths. For these runs, we report on total absorption, resonant
absorption, backscatter, specular reflection, maximum electron temper-
ature, flux limitation $f = Q/nmV_e^3$ at the critical density and maximum
ion expansion velocity between $0.1\ n_c$ and n_c during the course of the
runs. The laser pulse intensities vary in peak value (maximum inten-
sity) and in temporal distribution. In the following, short pulses
will refer to a Gaussian pulse shape with a FWHM of 75 psec for Nd and
750 psec for CO_2 light; a long pulse essentially looks the same until
it reaches its peak (50 psec for Nd; 500 psec for CO_2) when the
intensity is kept a constant. The initial density gradients belong to
two different categories: a) the constant density gradient below
critical density; b) the double structure density gradient. The idea
behind this classification is the following. At $t = 0$, it is assumed
that the surface material of the target has already been ablated by the
laser light for a very short time compared to the pulse length. In
case of the short pulse, it is assumed that a 10μ density gradient
scale length for Nd laser light is present when the pulse is turned on
(100μ for CO_2 light); for a long pulse it is assumed that a 100μ
density gradient scale length had time to form in front of the target
(1000μ for CO_2 laser). These define the constant density gradient
cases. For the double structure density gradient, it is assumed that
the target has been hit by a prepulse sometime before the arrival of

29

the pulse under consideration (main pulse). In this particular situation, we choose typically a 30μ density gradient scale length below n_c down to $0.1\ n_c$, and a 100μ density gradient scale length below $0.1\ n_c$. This density structure is in reasonable agreement with that measured by interferometry for a target irradiated with a prepulse.[3] No such runs were performed for CO_2 laser lights.

This double-structure density gradient is an artifice for simulating a prepulse because it proved to be inefficient to run a real prepulse case with the pulse and prepulse separated by 2 or 3 nsec. Also 2D effects might become important on this time scale. For all the runs in this section, the following parameters were set at the values of 0.3 for α (fractional resonant absorption once the light reaches critical density), and 0.1 for $e\phi/T_e$. Also all the runs reported, except when mentioned otherwise, have been made for polyethylene targets with a maximum Z of 2.67.

A. Single Short Pulses

In these runs, because of the shorter density gradient scale length, backscatter is expected to be unimportant. This is what the experiments show, in any case. A typical solution obtained at the peak of the laser pulse for 3×10^{15} W/cm^2 is shown in Fig. 2. On the electron density curve, let us note a lower density shelf forming above $0.5\ n_c$. The electron temperature profile shows a maximum in the lower density region around 7 keV. The ion temperature presents some structure. The maximum near the critical density is due to anomalous

30

energy transfer between electrons and ions. The bumps at lower
densities are usually a residual of backscatter in that region. Most
of the plasma is unstable to ion-acoustic instability and the flux
inhibition factor shows a maximum in the underdense region (minimum
inhibition). Above 0.1 n_c, it is first negative which corresponds to
a negative value of Q_e ($\frac{\partial T_e}{\partial x}$ > 0). It then goes as low as 10^{-3}, goes
up again as the density increases and reaches a maximum value above
critical density and tapers off around 0.3. This constitutes a fairly
typical behavior for f. Notice that the ion acoustic turbulence not
only limits the thermal flux in the underdense plasma, but also limits
it up to about 10µ into the overdense plasma also. At sufficiently
high density, the thermal flux becomes classical again. The
number for f which is reported in all the following figures is
taken at n = n_c. Finally, the fluid velocity (which is not shown)
reaches a maximum value of 1.4 10^8 cm/sec(corresponding to 50 keV ions)
at n = 0.1 n_c. At this point in time, the absorption for this case
was 38%, 25% of which was due to resonant absorption. A fraction of
9% had been backscattered whereas 52% had been specularly reflected.
The variation of these quantities with laser intensities is shown in
Fig. 3. From this figure, we see that the total absorption remains
roughly constant, around 40%, over 2 orders of magnitude in intensity.
The resonant absorption is responsible for more than half of the total
absorption (around 25%). Only above 10^{16} W/cm^2, does the backscatter
increase, the resonant absorption drops leading to a decrease in total
absorption. This calculated absorption of 40% is in reasonable

agreement with short pulse experiments on low Z targets at both NRL[49] and Livermore.[12] Figure 4 shows maximum electron temperature, ion blowoff velocity and flux limit at $n = n_c$ as a function of irradiance. Also plotted as individual points on this figure are values of hot electron temperature which were measured at the Naval Research Laboratory[50] for 75 psec Gaussian pulses on polyethylene targets.

B. Long Pulses

Our simulations of long pulse experiments in Nd laser produced plasma generally show that there is an initial transient during which the plasma settles down. This treatment typically lasts for tens of picoseconds, and is usually characterized by strong Brillouin back-scatter. The duration of this transient period increases with irradiance. For instance it is less than 50 psec for 10^{14} W/cm^2 and is about 70 psec for 10^{15} W/cm^2. After this, the plasma settles down into a much steadier state (for typically 50-150 psec until the end of the run) as far as absorption is concerned. The ions however accelerate throughout the run, so maximum ion velocity may actually be larger than shown here. All of the results we quote here are for the latter part of the pulse.

The total absorption is larger in these long pulse experiments than in the case of short pulse experiments, probably because the ion-acoustic turbulence has much more space to grow on these large density scale lengths. Also, because the absorption takes place in this manner, less light actually gets to the critical region and the percentage for resonant absorption is smaller than for single short

32

pulse experiments. The absorption physics is then dominated by the complicated interplay, in the underdense region, between classical and/or anomalous absorption, and backscatter.

In Fig. 5 are plotted absorption, resonant absorption, back-scatter and specular reflection as a function of irradiance from $3 \times 10^{12} - 1.5 \times 10^{15} W/cm^2$. Experimental results on total absorption are shown as circles for the NRL long pulse experiment[5], and as squares for the Sandia long pulse experiment.[51] At low irradiance, the absorption is classical and no instabilities are excited. At higher irradiance, both ion acoustic turbulence and backscatter are important. As a rule of thumb, the transition from classical to anomalous behavior occurs above 10^{14} W/cm^2, at which point the total absorption is 80%, but absorption due to ion acoustic turbulence is 13% (which was measured by redoing the calculation with return current driven ion acoustic instability turned off), resonant absorption is 16% and fraction backscattered is 3%. At 7×10^{14} W/cm^2, the anomalous absorption (measured in the same way) is 54% out of a total of 66% with 12% resonant absorption and 15% backscatter.

In Fig. 6 are shown maximum electron temperature, ion blow-off velocity and flux limit as a function of irradiance. Note that at 7×10^{14} W/cm^2, the maximum temperature 7.5 keV compares reasonably well with the nonthermal tail temperature of 10 keV quoted in Ref. 5. The picture which emerges from these calculations is that at high irradiance, the nonthermal tail on the integrated x-ray distribution

comes from a thermal plasma at low (roughly critical) density, while the lower temperature x-radiation is from the denser, cooler plasma.

C. Double-structure Density Gradient

An easy way to simulate numerically a prepulse is by introducing a double density gradient scale length. We chose 30 and 100μ for the standard case.[3] Results for this case appear in Fig. 7 and 8. Also plotted are experimental results for backscatter[4] for laser irradiance varying between 10^{15} and 10^{16} W/cm^2. The results of Ref. 4 are corrected to account for the fact that our simulations are with a given prepulse, not a given prepulse to main pulse ratio.[6]

An interesting feature of these results is the maximum electron temperature observed in the runs. In these runs, the main pulse is of a short pulse type. Once backscatter becomes important, the light does not reach the critical region and the electron temperature does not increase any more. Also, the light does not have time to burn its way through to the critical density region. The incident laser energy is delivered instead to the ions which become very energetic (2 x 10^8 cm/sec or 100 keV ions). This feature could be used for applications which will be mentioned later.

Another dependence of the double-structure density gradient was investigated. Instead of using 30μ on the density gradient scale length near the critical surface, 10μ to 50μ was tried instead. This variation was thought to mock-up a variation in strength of prepulse and/or variation in delay time. Results are shown in Fig. 9. The main result from this series of runs is the small variation observed

34

due to changes of this parameter. This feature also is consistent with the experimental results.[4] To summarize, both our simulations and the experiment show a strong increase in backscatter with increase in irradiance for double structure pulses, and a much weaker increase in backscatter as strength of prepulse to main pulse increases and/or delay time increases (when x varies from 30 to 50μ for example).

D. Different Elements

Sensitivity of absorption and other quantities to various elements was considered. We chose aluminum instead of polyethylene as another target material in order to consider the largest possible variation in target element without introducing unnecessary complications due to the radiation processes. It was expected that if the temperature reached 5 keV, Al should be fully ionized and as a result, only bremsstrahlung losses needed to be taken into account, like in our present version of the code. A test was made with Al at 10^{15} W/cm^2 for a short pulse and a double-structure density gradient. The results obtained were extremely close quantitatively to those obtained for a CH_2 target for all the quantities plotted. This proves that classical inverse bremsstrahlung plays a very insignificant role since it is five times stronger at that laser irradiance for aluminum than for CH_2 but the absorption and temperature stay the same.

E. Different Laser Wavelengths

All of the runs reported above were obtained for the case of Nd laser light (λ = 1.06μ). Runs were also performed for light of other wavelength. Our most extensive set of runs is for a CO_2 (λ = 10.6μ) laser produced CH_2 plasma. To do so, scale lengths and times for the short and long pulses of a Nd laser plasma were multiplied by ten and irradiances were divided by 100. Results appear in Fig. 10 and 11 for short pulses and in Fig. 12 and 13 for long pulses. Overall, results are quite similar to those obtained for Nd light. Backscatter is observed, both in the cases of short and long pulse experiments. Comparable levels are reached for slightly larger values of $I\lambda^2$ for CO_2 than for Nd laser light, and for the short pulse configuration, absorption by ion acoustic turbulence is somewhat less than it is for a Nd laser plasma. Notice that for long pulses our calculation predicts good absorption to irradiances beyond 10^{13} W/cm^2.

To test the effect of a shorter wavelength, two other simulations were done, one at 0.53μ for a CH_2 plasma at an irradiance of 10^{15} W/cm^2 which we could compare to an experiment,[52] and one at 0.26μ for a CH_2 plasma at 10^{16} W/cm^2. In the first case, the laser pulse width at half-maximum was taken to be 70 psec whereas it was shortened to 40 psec in the second case. The initial density gradient scale length was chosen to be 5μ but it was observed that in both cases, by the end of the pulse it was more like 15-20μ. For the 0.53μ case, total absorption was 47% vs. 45% reported experimentally. The maximum electron temperature obtained numerically was 2.9 keV vs. 2 keV

36

measured from a hard X-ray spectrum. The maximum blowoff velocity was $1.1 \ 10^8$ cm/sec and the flux limit was 0.1. It was also found in our computation that a fraction of 23% was resonantly absorbed and 6% only was backscattered. For the 0.26μ case, the total absorption was further enhanced to 54% with the contribution of the resonant absorption remaining steady at 23%. The specular reflection reached 42% and backscatter diminished to 4%. The maximum temperature was 6.5 keV, blowoff velocity $1.5 \ 10^8$ cm/sec and flux limit f = 0.1. Thus as the wavelength is shortened, most of the absorption increase comes from an enhancement of the absorption due to ion acoustic instability and inverse bremsstrahlung.

As a final example we consider millimeter sources. For instance the NRL gyrotron produces about 150 kW at a wavelength of 8mm.[53] The critical density is $n_c = 1.6 \times 10^{13}$ cm^{-3}. Assuming that the beam can be collimated to a 5 cm radius, this corresponds to an irradiance of 2×10^3 W/cm^2, which is about 20 times higher than the f = 1 thermal flux $n_c m V_e^3$ for a 1 eV plasma. We have simulated this case for a 1 eV hydrogen plasma for a 'short pulse', where the gradient scale length is 8 cm and the pulse width is 600 nanoseconds. The total absorption is 35%, resonant absorption is 29%, specular reflection is 65% and there is no backscatter. At the critical density the electron temperature increased to about 18 eV but there was no heating anywhere else. The return current driven ion acoustic instability was not excited anywhere. Although it is unphysical, we also simulated a 'long pulse' at 2×10^3 W/cm^3 with an initial density gradient scale

37

length of 80 cm for a total time of 0.8μsec. (This is unphysical because the beam radius is less than one tenth of the gradient scale length; two dimensional effects should be very important). The absorption is much greater, about 79%, but it is all resonant absorption (17%) and inverse bremsstrahlung; again the return current driven ion acoustic instability is not excited anywhere. Thus our simulations give the result that millimeter wave plasma interactions (and presumably microwave plasma interactions also) do not give rise to a return current driven ion acoustic instability.

VI. Suggestions for Further Experiments

A. Varying Pulse Shape to Optimize Absorption

We have attempted to optimize the light absorption by varying the laser pulse shape. In all cases the laser system was operated in a long pulse mode with an initial density gradient scale length of 100μm and an average irradiance of 1.5×10^{15} W/cm^2. Two periods of the six pulse shapes we used are shown in Fig. 14. For a uniform laser pulse (a), the fractional absorption was 67% after the system reached steady state.

Next we studied the effect of varying the laser irradiance with time by selecting several periodic pulses with period of 100psec. All absorption efficiencies we quote are averaged over a time of 100psec which was taken to begin after the initial transients died

away. First we tried to see whether relatively small changes in pulse shape could have a significant effect. To test this out we tried two sawtooth oscillations, first (B) an abrupt rise to 2.25×10^{15} W/cm^2 and a linear fall-off to 0.75×10^{15} W/cm^2 in a hundred psec; and second, (C) an abrupt fall to 0.75×10^{15} W/cm^2 followed by a linear rise to 2.25×10^{15} W/cm^2 followed by a linear rise to 2.25×10^{15} W/cm^2 in 100 psec. The absorption efficiency for the former was 62% and for the latter was 59%.

Since relatively small perturbations in the waveform did not have a significant effect on absorption, we tried larger perturbations. First, the irradiance (D) was set at 3×10^{14} W/cm^2 for the first 20 psec and then raised to 1.8×10^{15} W/cm^2 for the last 80 psec. Second, the irradiance (E) was raised to 5×10^{15} W/cm^2 for 20 psec and then lowered to $.625 \times 10^{14}$ W/cm^2 for the remaining 80 psec. Finally, the irradiance (F) was raised to 5×10^{15} W/cm^2 for 5 psec and then lowered to $(\frac{25}{19}) \times 10^{15}$ W/cm^2 for the remaining 95 psec. The fractional absorptions were respectively 44%, 46% and 56%. Thus violently changing the pulse shape appears to be quite harmful for fractional absorption. The best absorption is then predicted to result from as smooth and clean a pulse as possible.

This result may have application to recent experiments which tested the fractional absorption as a function of position of the target with respect to the focal point of the lens.[6,7] The best

absorption occurred for the target in the focal plane. In the NRL experiment,[6] the beam quality was also measured as a function of distance from focal plane. At best focus, the beam quality was by far the best. The curves of constant intensity were simple closed curves, one closed curve for each intensity. Further from the focal plane, the laser light had many more hot spots and the beam quality was much worse. If these hot spots in space behave the same as the hot spots in time which we simulated, the fractional absorption should maximize for the target at the focal plane.

B. Further Studies of Resonant Absorption

Recently, Manes et al[54] have performed short pulse experiments to study resonant absorption. By tilting the target for s and p polarized light, they found a maximum absorption where the theory of resonant absorption predicts. According to our simulations, resonant absorption is the dominant mechanism for short pulse experiments. However for long pulse and double structure pulse experiments, it plays a less important role. Therefore we feel that it would be interesting to repeat this experiment where the laser is run in a long pulse or double structured pulse mode at an irradiance of perhaps 10^{15} W/cm^2. If our model is correct, there should be less evidence for resonant absorption.

C. Production of a Dense, Hot Ion Plasma

As we have seen in the last section, once the irradiance increases above 10^{16} W/cm^2 for a double structured laser pulse, the absorption is predicted to drop drastically due to the Brillouin

40

backscatter. However a fraction of the incident laser energy equal to roughly $2 ((T_e + 3 T_e)/Mc^2)^{1/2}$ is deposited directly into the ions by the backscatter instability. For irradiances of order 10^{17} W/cm^2 our code predicts almost complete backscatter and an _ion_ temperature of ten to twenty keV for the entire underdense plasma. (However the electron temperature is much smaller).

This result suggests that it might be possible to produce a dense ($n_e \sim 10^{20} - 10^{21}$ cm^{-3}) plasma with very high ion temperature. We do not believe any other plasma source at this density and ion temperature exists. For one thing this plasma could serve as a very compact thermal source of thermonuclear reaction products. To test this idea, we have run our code on a double structured plasma produced by a prepulse. The scale length is 100 μm for $n_e < 10^{20}$ and is 30μm for $10^{20} < n_e < 10^{21}$. This plasma is then irradiated with a 75 psec FWHM Gaussian pulse with a maximum irradiance of 2×10^{17} W/cm^2, like that discussed in Section V. For a D-T plasma, the ion temperature reaches a maximum of 15 keV and for $n_e < 10^{22}$ cm^{-3} is everywhere greater than 7keV at the peak of the pulse. The total number of neutrons produced is 4.8×10^{13} /cm^2 and the total energy in reaction products is 136 J/cm^2 as compared to laser input energy of 1.07×10^5 J/cm^2. The plasma is so hot and dense that it can even serve as a source of advanced reaction products. For instance we have rerun the calculation for a D-H$_e$^{3} plasma. The output is now 1.4×10^{12} protons/cm^2, or 3.94 J/cm^2 of reaction products.

Although this theoretical result is admittedly quite specu-
lative, there are at least two reasons (other than our code results)
to believe it may be true. First of all, it is well established
theoretically that Brillouin scattering does ultimately deposit energy
$2 V_s/c$ times the laser energy directly into the ions. Secondly, the
experimental results of Ripin and McLean[4] show that for a double
structured plasma, the backscatter increases with irradiance. For
instance the plot of backscattered energy versus laser energy (Fig. 3
of Ref. 4) shows no indication of saturation, and at an irradiance of
10^{16} W/cm^2 (the highest irradiance shown) 50% of the energy is back-
scattered. If this trend continues for irradiance of 10^{17} W/cm^2,
which seems likely, and if the backscatter is due to stimulated
Brillouin backscatter, which also seems likely, then there is really
no way to avoid producing this dense hot ion plasma. On the other
hand, for such a large laser energy input, the value of the trapping
width compared to thermal velocity (Eq. (8)) was calculated to be
much larger than for our other simulations. Hence the ion wave may
be driven into a highly nonlinear regime, and conventional wave-
breaking could also be playing an important role. In any case, it
seems to us that irradiating a prepulse produced plasma with a main
pulse of 10^{17} W/cm^2 would be a very interesting experiment.

VII. Conclusions

We conclude, from the evidence presented here, that fluid
simulation with anomalous transport, is an accurate and cost effec-
tive way to describe the absorption, backscatter and flux limitation

in a laser produced plasma. Our calculations give quantitatively
correct absorption of laser light over five orders of magnitude in
irradiance, for short pulses, long pulses, and double structured
pulses.

There are at least two results of our calculation which may have
direct application to laser fusion. First, the absorption appears to
maximize for smooth, clean pulses. This obviously indicates that a
high quality laser and focusing system will give best results. Second,
if low irradiance, long pulses prove to be a viable approach to laser
fusion,[5,55] a CO_2 laser with an irradiance of about 10^{13} W/cm^2 could
be very attractive. Although the absorption efficiency is only about
half that of a Nd laser at the same irradiance, its efficiency is
much more than twice as great, so more of the _input_ energy to the
laser is coupled to the pellet. The maximum electron temperature for
this CO_2 laser produced plasma is about 5 keV. However this is the
temperature only at the critical density. At $n \sim 10^{21}$ cm^{-3}, the
temperature is typically around 1 keV.

References

1. W. M. Manheimer, D. G. Colombant and B. H. Ripin, Phys. Rev. Lett. 38, 1135 (1977).

2. W. M. Manheimer and D. G. Colombant, Phys. Fluids 21, 1818 (1978).

3. B. H. Ripin, F. C. Young, J. A. Stamper, C. M. Armstrong, R. Decoste, E. A. McLean and S. E. Bodner, Phys. Rev. Lett. 39, 611 (1977).

4. B. H. Ripin and E. A. McLean, NRL Memo Report 3964 (1979); to be published in Appl. Phys. Lett.

5. B. H. Ripin, R. R. Whitlock, F. C. Young, S. P. Obenschain, E. A. McLean and R. Decoste, NRL Memo Report 3965 (1979); B. H. Ripin, R. Decoste, S. P. Obenschain, S. E. Bodner, E. A. McLean, F. C. Young, R. R. Whitlock, C. M. Armstrong, J. Grun, J. A. Stamper, S. H. Gold, D. J. Nagel, R. H. Lehmberg, and J. M. McMahon, to be published in Phys. Fluids.

6. B. H. Ripin, NRL Memo Report 3684 (1977).

7. C. G. M. Van Kessel, J. N. Olsen, P. Sachsenmaier, R. Sigel, K. Eidmann and R. P. Godwin, presented at the 10th European Conf. on Laser Interaction with Matter, Ecole Polytechnique, Palaiseau, France (1976).

8. J. P. Freidberg, R. W. Mitchell, R. L. Morse and L. J. Rudinski, Phys. Rev. Lett. 28, 795 (1972).

9. D. W. Forslund, J. M. Kindel, K. Lee, E. L. Lindman and R. L. Morse, Phys. Rev. A 11, 679 (1975).

10. K. G. Estabrook, E. J. Valeo and W. L. Kruer, Phys. Fluids 18, 1151 (1975).

11. D. W. Forslund, J. M. Kindel and E. L. Lindman, Phys. Fluids 18, 1017 (1975).

12. R. A. Haas, W. C. Mead, W. L. Kruer, D. W. Phillion, H. N. Kornblum, J. D. Lindl, D. MacQuigg, V. C. Rupert, and K. G. Tirsell, Phys. Fluids 20, 322 (1977).

13. H. D. Shay, R. A. Haas, W. L. Kruer, M. J. Boyle, D. W. Phillion, V. C. Rupert, H. N. Kornblum, F. Rainer, V. W. Slivinsky, L. N. Koppel, L. Richards, and K. G. Tirsell, Phys. Fluids 21, 1634 (1978).

14. M. D. Rosen, D. W. Phillion, V. C. Rupert, W. C. Mead, W. L. Kruer, J. J. Thomson, H. N. Kornblum, V. W. Slivinsky, G. J. Caporaso, M. J. Boyle and K. G. Tirsell, Preprint UCRL - 82146 (1978).

15. G. Zimmerman and W. L. Kruer, Comm. Plasma Phys. 2, 85 (1975); G. B. Zimmerman, Lawrence Livermore Laboratory Report No. UCRL-74811, 1973 (unpublished).

16. W. M. Manheimer, Phys. Fluids 20, 265 (1977).

17. W. M. Manheimer, C. E. Max, and J. J. Thomson, Phys. Fluids 21, 2009 (1978).

18. R. Faehl and W. L. Kruer, Phys. Fluids 20, 55 (1977).

19. A. Mase and T. Tsukishima, Phys. Fluids 18, 464 (1975).

20. C. C. Daughney, L. S. Holmes and J. W. M. Paul, Phys. Rev. Lett. 25, 497 (1970).

21. K. Muraoka, E. L. Murray, J. M. W. Paul and D. R. Summers, J. Plasma Phys. 10, 135 (1973).

22. Y. Kowai and M. Guyot, Phys. Rev. Lett. $\underline{39}$, 1141 (1977).

23. S. M. Hamburger and J. Jancarik, Phys. Fluids $\underline{15}$, 825 (1972).

24. R. E. Slusher, C. M. Surko, D. R. Moler and M. Porkolab, Phys. Rev. Lett. $\underline{36}$, 674 (1976).

25. A. Y. Wong, B. H. Quon and B. H. Ripin, Phys. Rev. Lett. $\underline{30}$, 1299 (1973).

26. B. H. Quon, A. Y. Wong and B. H. Ripin, Phys. Rev. Lett. $\underline{32}$, 406 (1974).

27. M. Lampe, W. M. Manheimer, J. B. McBride, J. H. Orens, R. Shanny, and R. Sudan, Phys. Rev. Lett. $\underline{26}$, 1221 (1971).

28. M. Lampe, W. M. Manheimer, J. B. McBride, J. H. Orens, K. Papadopoulos, R. Shanny and R. N. Sudan, Phys. Fluids $\underline{15}$, 662 (1972).

29. M. Lampe, W. M. Manheimer, J. B. McBride, and J. H. Orens, Phys. Fluids $\underline{15}$, 2356 (1972).

30. M. Lampe, I. Haber, J. H. Orens and J. P. Boris, Phys. Fluids $\underline{17}$, 428 (1974).

31. J. A. Wesson, A. Sykes and H. R. Lewis, Plasma Phys. $\underline{15}$, 49 (1973).

32. D. Biskamp and R. Chodura, Phys. Fluids $\underline{16}$, 893 (1973).

33. D. Biskamp, K. U. von Hagenow and H. Welter, Phys. Lett. $\underline{39A}$, 351 (1972).

34. C. T. Dum, Phys. Fluids $\underline{21}$, 956 (1978).

35. M. Z. Caponi and R. C. Davidson, Phys. Rev. Lett. $\underline{31}$, 86 (1973).

36. A. M. Sleeper, J. Weinstock and B. Bezzerides, Phys. Fluids $\underline{16}$, 1508 (1973).

37. W. M. Manheimer and R. Flynn, Phys. Fluids 17, 409 (1974).

38. D. Choi and W. Horton, Phys. Fluids 17, 2048 (1974).

39. M. N. Rosenbluth, Phys. Rev. Lett. 29, 565 (1972).

40. K. Nishikawa and C. S. Liu in Advances in Plasma Physics, Vol. 6 Wiley & Sons (1976).

41. M. N. Rosenbluth, R. P. White, and C. S. Liu, Phys. Rev. Lett. 31, 1190 (1973).

42. W. M. Manheimer, Phys. Fluids 17, 1634 (1974).

43. D. W. Phillion, W. L. Kruer, and V. C. Rupert, Phys. Rev. Lett. 37, 1529 (1977).

44. C. L. Tang, J. Appl. Phys. 38, 390 (1967).

45. W. M. Manheimer and H. H. Klein, Phys. Fluids 17, 1889 (1974).

46. P. M. Campbell, R. R. Johnson, F. J. Mayer, L. V. Powers, and D. C. Slater, Phys. Rev. Lett. 39, 274 (1977); R. L. Morse and R. C. Malone, Bull. Am. Phys. Soc. 21, 1028 (1976).

47. J. M. Dawson and C. Oberman, Phys. Fluids 6, 394 (1963).

48. K. Lee, D. Forslund, J. M. Kindel and E. L. Lindman, Phys. Fluids 20, 51 (1977).

49. B. H. Ripin, Appl. Phys. Lett. 30, 136 (1977).

50. F. C. Young and B. H. Ripin, Bull. Am. Phys. Soc. 22, 1112 (1977) submitted for publication.

51. J. P. Anthes, M. A. Palmer, M. A. Gusinow and M. K. Matzen, Bull. Am. Phys. Soc. 23, 777 (1978).

52. F. Amiranoff, R. Benattar, R. Fabro, E. Fabre, C. Garban, C. Popovics, A. Poqueruse, R. Sigel, C. Stenz, J. Virmont and M. Weinfeld, in Plasma Physics and Controlled Thermonuclear Fusion (International Atomic Energy Agency, Vienna, 1978) (to be published).

53. M. Read, R. Gilgenbach, R. Lucey, K. R. Chu and V. L. Granastein, to be published.

54. K. R. Manes, V. C. Rupert, J. M. Auerbach, P. H. Y. Lee, and J. E. Swain, Phys. Rev. Lett. 39, 281 (1977).

55. NRL Laser-Plasma Interaction Group, NRL Memo Report 3890 (1978), ed. B. H. Ripin.

48

Appendix A

The code which is listed in the next appendix is a time-dependent one dimensional, one fluid hydrodynamic code with two temperatures. It uses an eulerian description of the fluid equations and uses FCT as its basis for the convection algorithm. It uses time-splitting techniques and all the convective terms are treated explicitly whereas the diffusive terms are treated implicitly. The hydrodynamic equations are very common and have received wide attention and coverage in the literature. Other equations are not so common and although they do not present formidable difficulties, care must be exercised when solving them in order for them to reflect the physics as accurately as possible.

In this code, the field equations received a special treatment because of the following fact as mentioned in section III; the coupling between Brillouin backscatter and the incident field is very strong and must be reflected in the algorithm. The amplitude of the Brillouin backscatter depend on the amplitude of the incident field intensity which is being solved for in the field equations. Fields at a previous time step cannot be used because they lead to an unstable situation. Where the incident field is large, the Brillouin back-scatter is large and as a result, the incident field drops very rapidly. On the next time step, the Brillouin backscatter is very small and the field penetrates much more readily. One more time step and the Brillouin backscatter is large again, making the laser light recede. In order to avoid this unphysical type of behavior, a

49

marching technique was used for solving Eq. (20) where the coefficient for Brillouin backscatter was computed at the previous location using the field just calculated there. This marching technique can lead to potential problems if it is not reversible. A marching technique typically uses values at the previous spatial point to advance the solution to the next point. Because we retrace our steps backwards in order to get the reflected intensity as well, the marching will take place using values ahead of the solution if we look at it from the point of view of the incident field calculation. This leads easily to irreversible solution which then could be interpreted as "numerical" absorption for the field equations.

The solution to this problem for the backscatter term as well as for the absorption term was to use the same value when going forward as when coming back. These terms were calculated at the middle of a cell and whatever the direction the calculation was proceeding, the change in the term in that cell was the same. Tests on reversibility were performed and found accurate to within one percent.
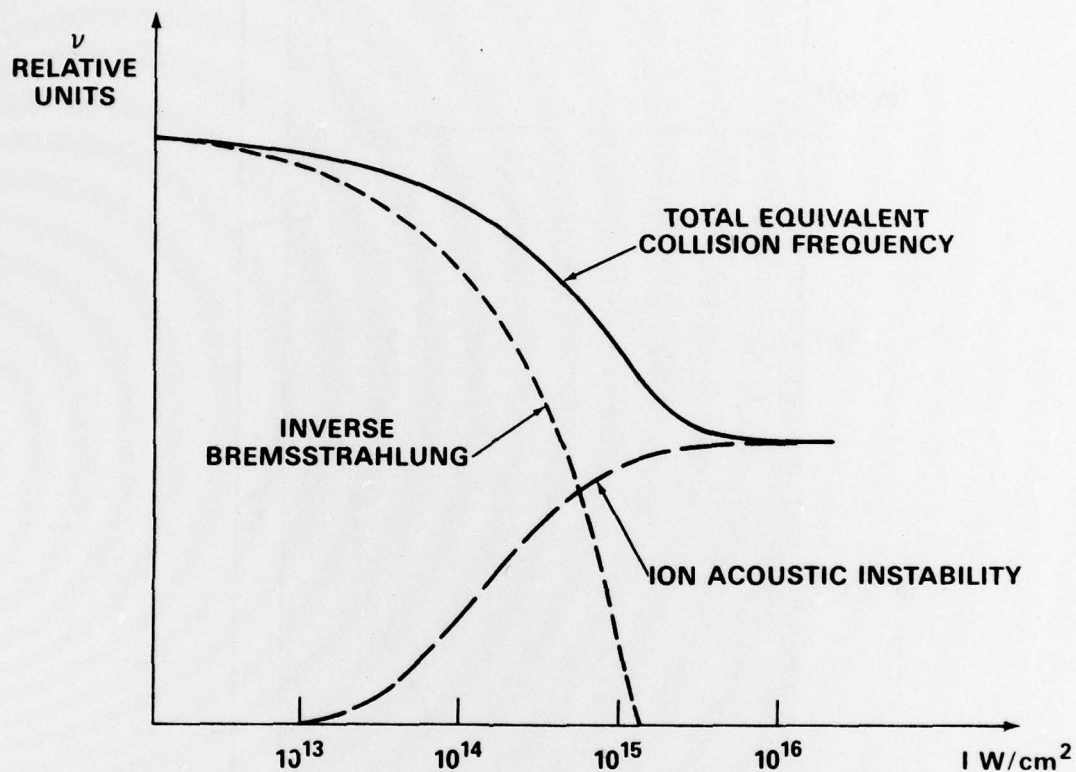
Fig. 1 – Schematic diagram of importance of inverse bremsstrahlung and ion acoustic turbulence as a function of irradiance (for Nd laser light)
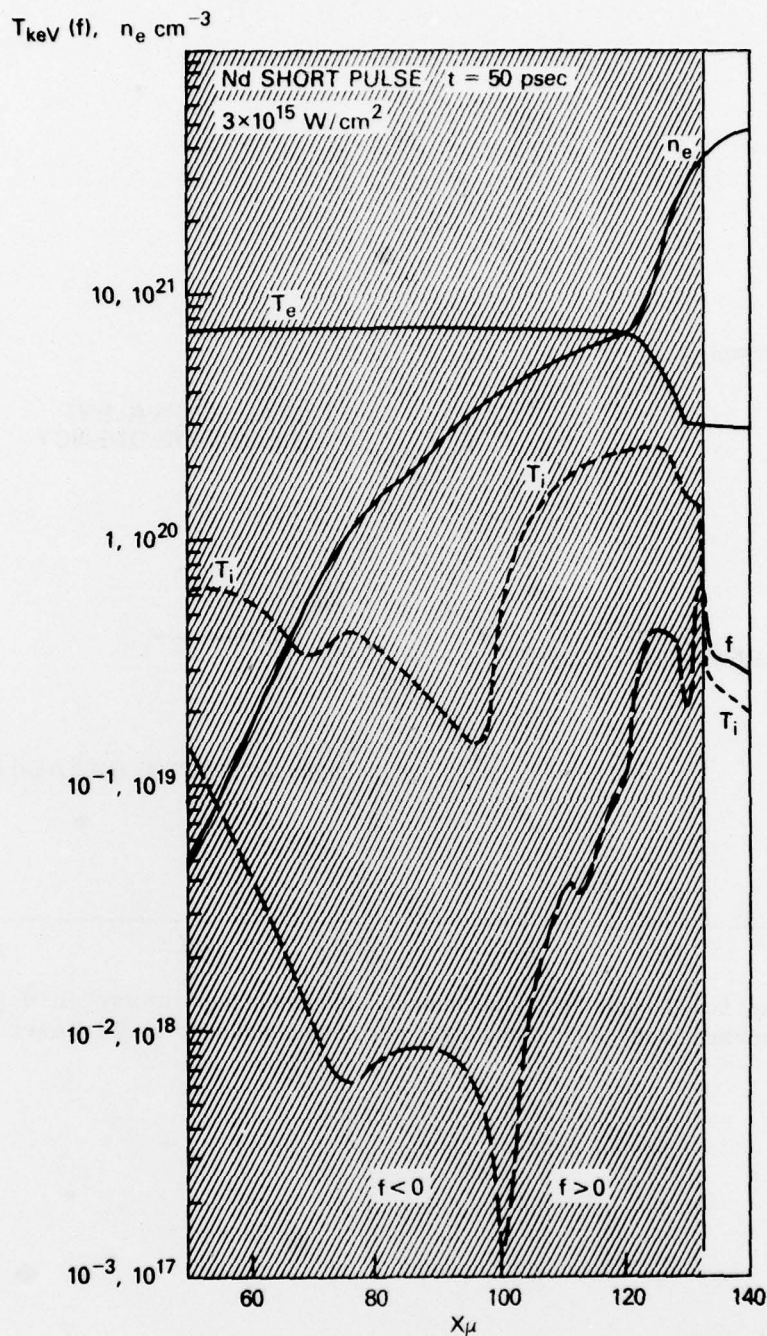
Fig. 2 - Spatial variation of density, electron and ion temperature, flux limit and incident and reflected fields at the peak of the Nd laser pulse for a Gaussian pulse 75 psec FWHM and maximum irradiance of 3×10^{15} W/cm^2 for polyethylene target. The shaded areas are unstable to return current generated ion turbulence.
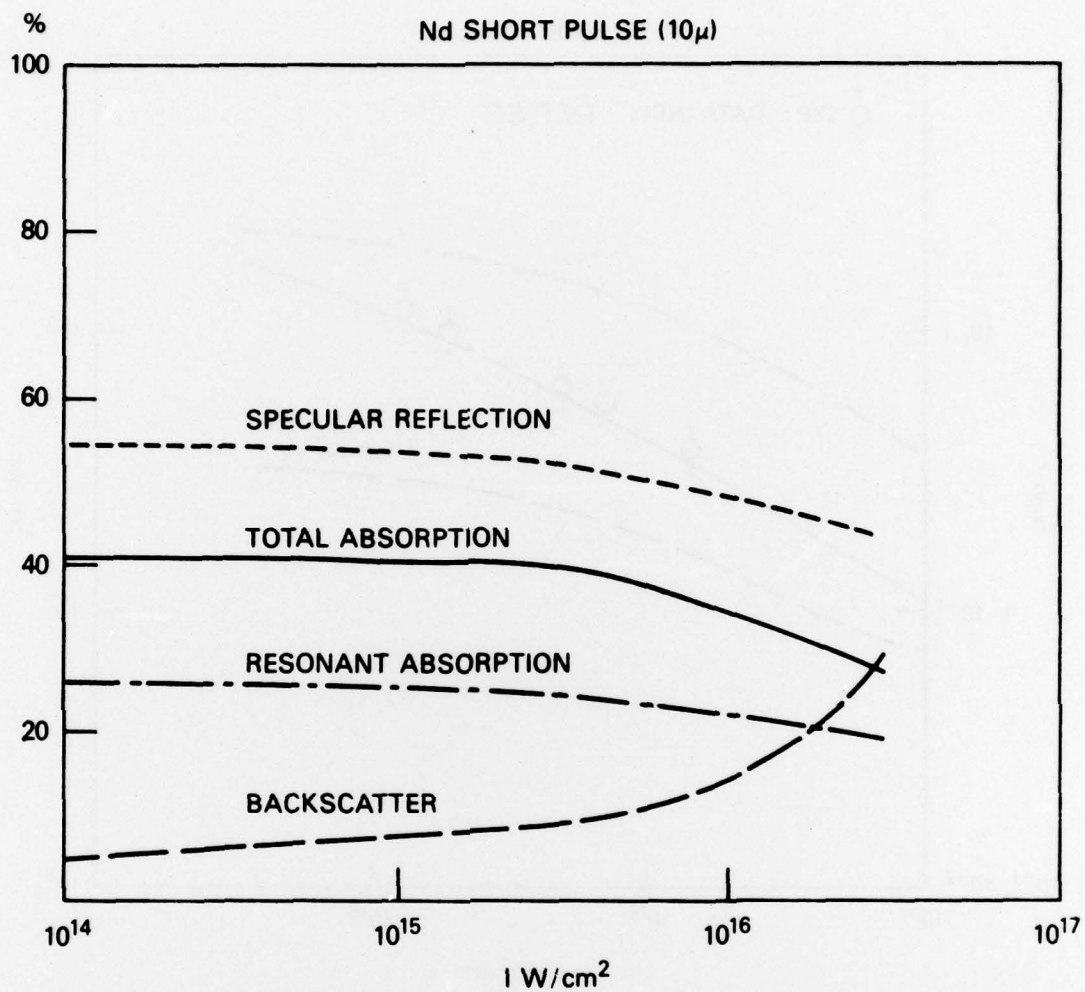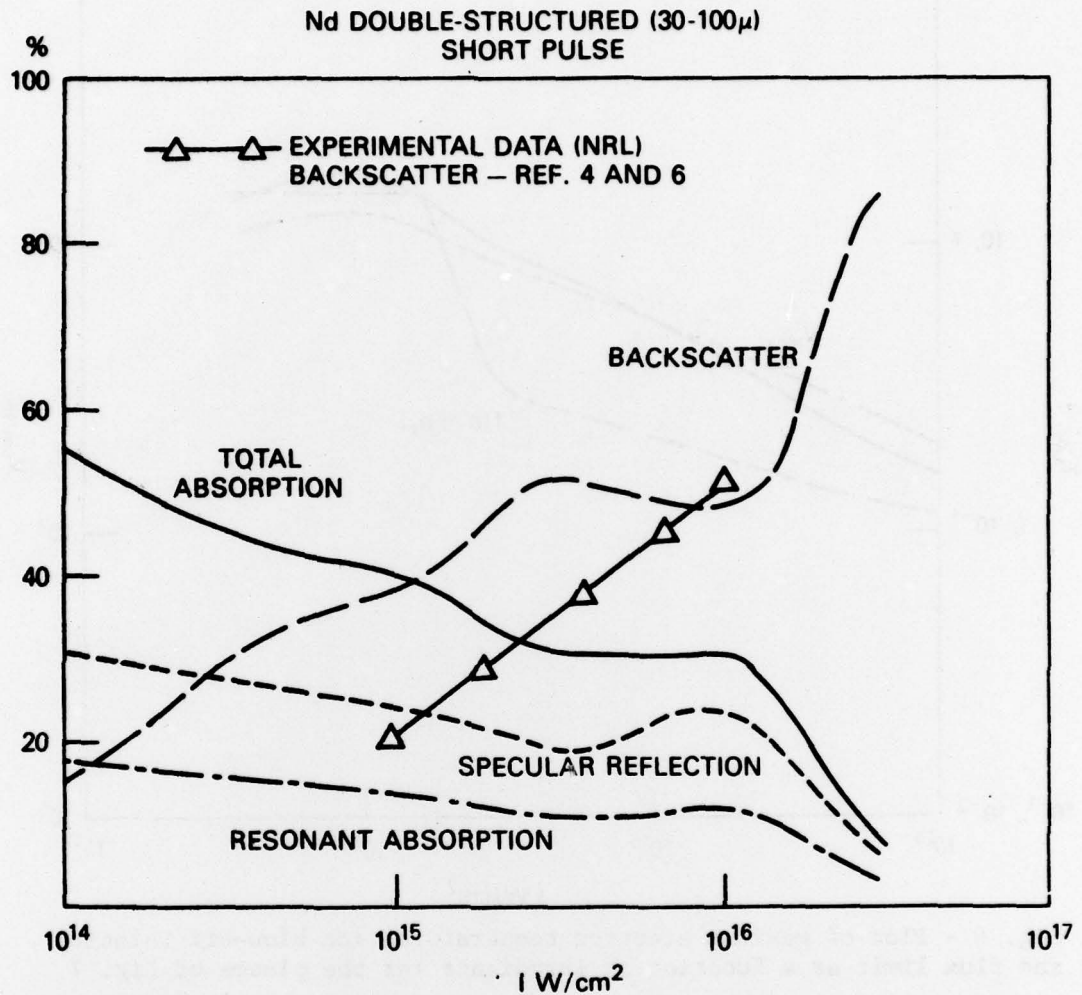
Fig. 3 - Plot of absorption, resonant absorption, specular reflection and backscatter as a function of irradiance for short pulse Nd laser plasma
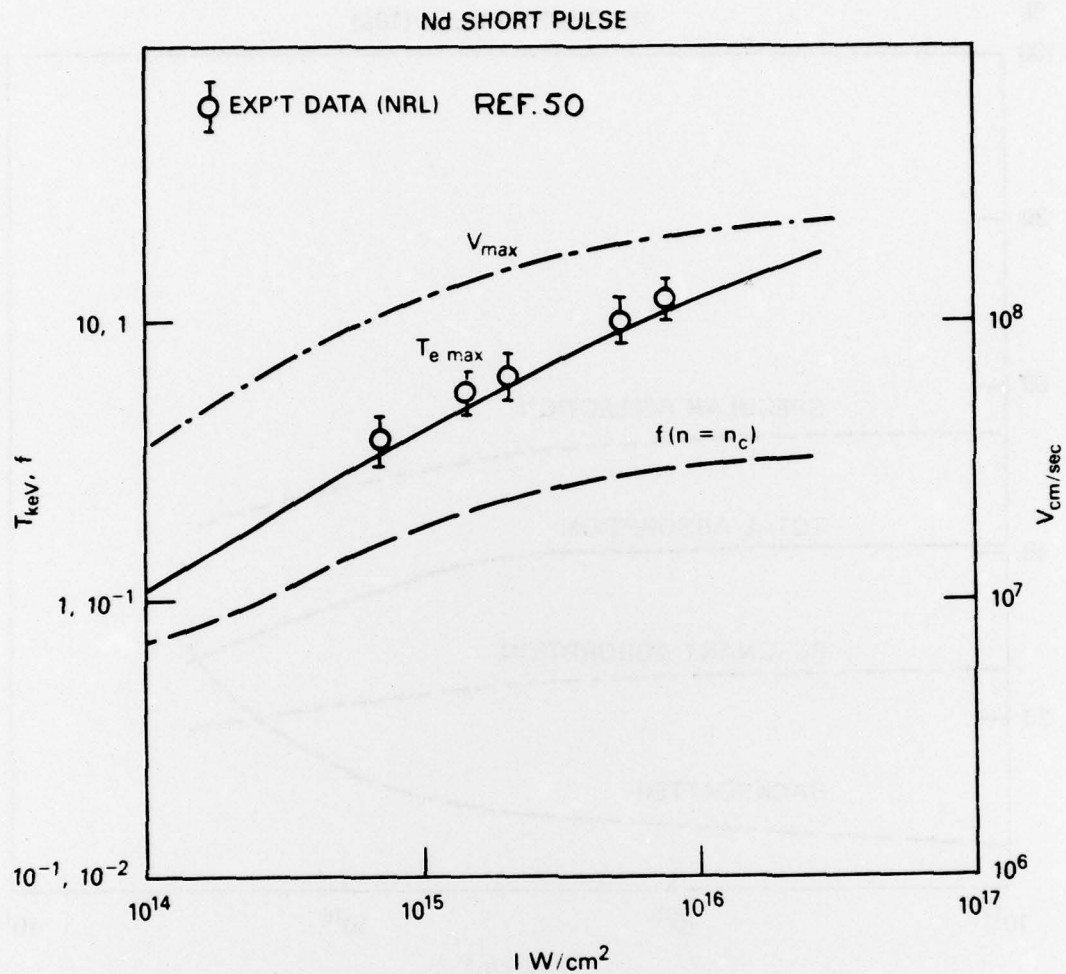
Fig. 4 - Plot of maximum electron temperature, flux limit at $n = n_c$ and blow-off velocity as a function of irradiance for the plasma of Fig. 3

54
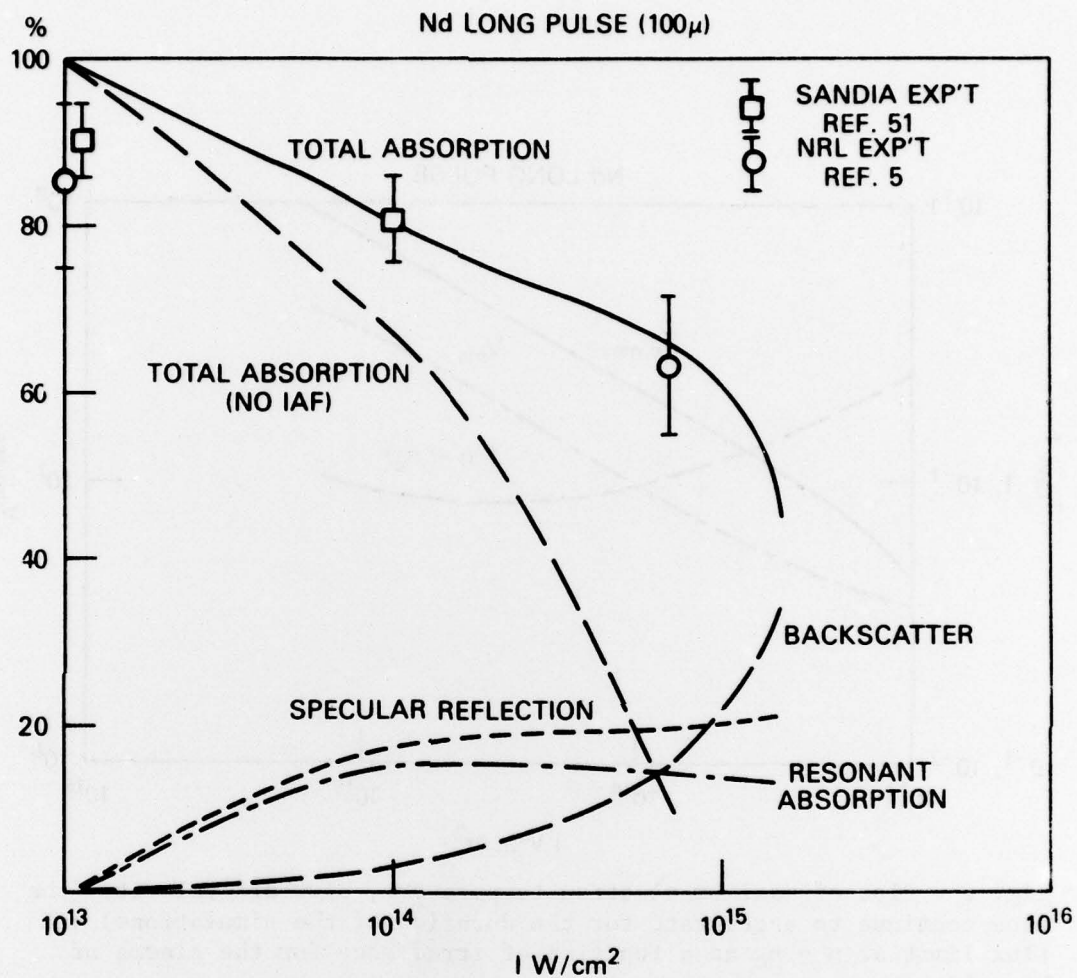
Fig. 5 - Plot of absorption, resonant absorption, specular reflection and backscatter as a function of irradiance for long pulse Nd laser plasmas. The circles are NRL data and the squares, Sandia data. The dashed total absorption curve shows total absorption without ion acoustic fluctuation contribution.
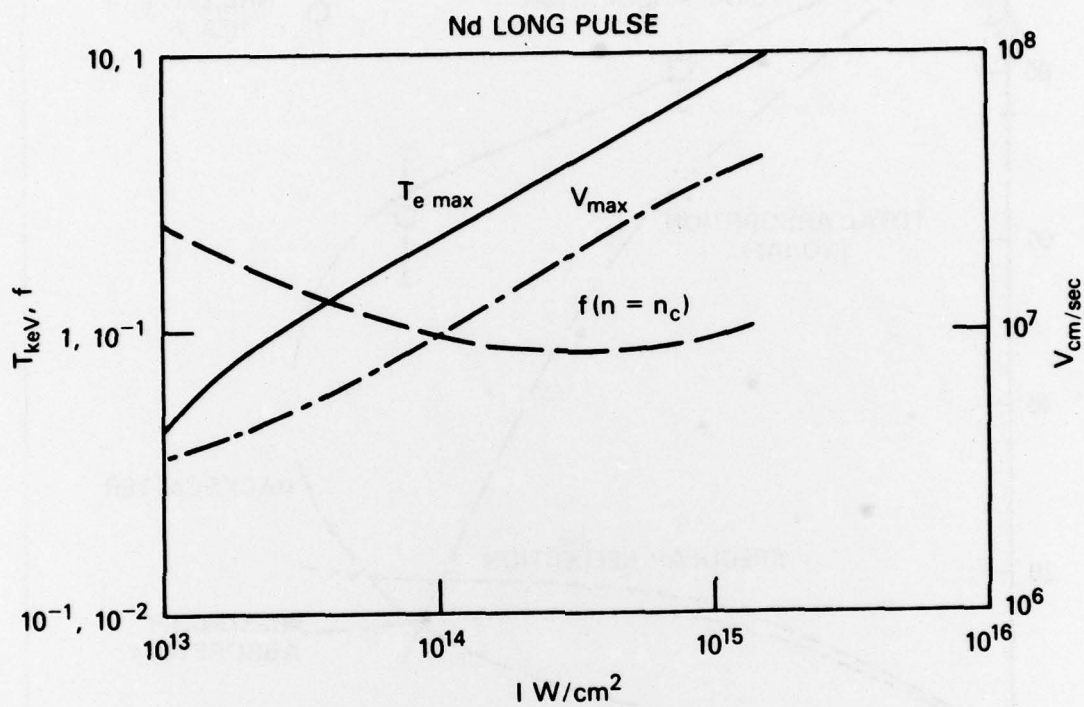
Fig. 6 - Plot of maximum electron temperature, blow-off velocity (the ions continue to accelerate for the duration of the simulations) and flux limit at $n = n_c$ as a function of irradiance for the plasma of Fig. 5
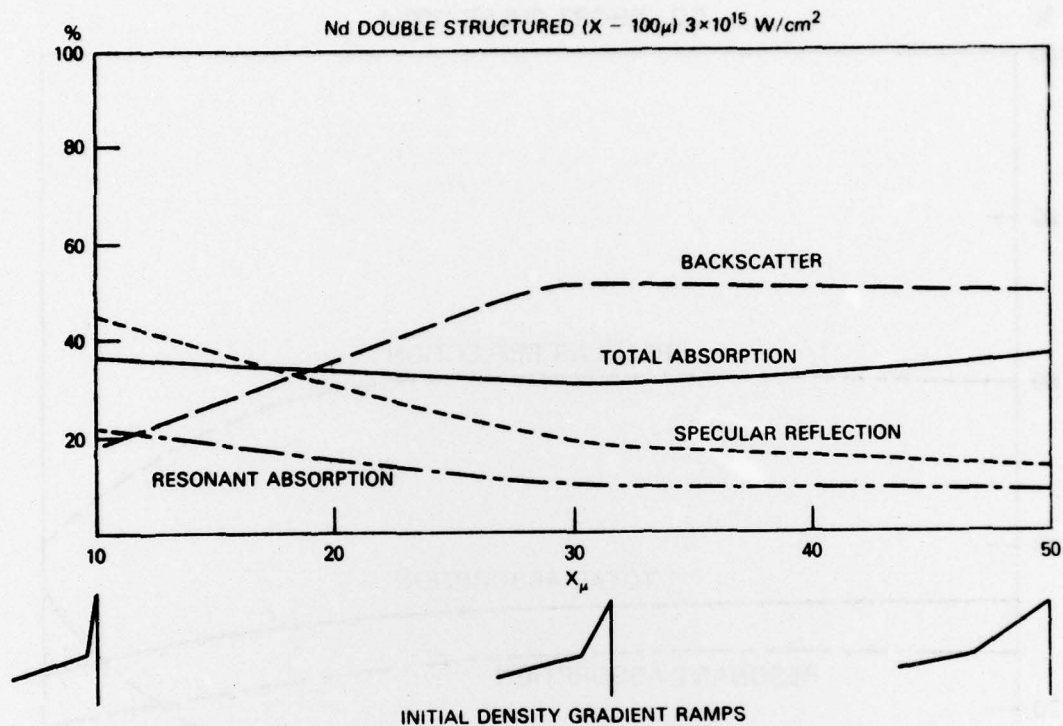
Nd DOUBLE-STRUCTURED (30-100μ)
SHORT PULSE
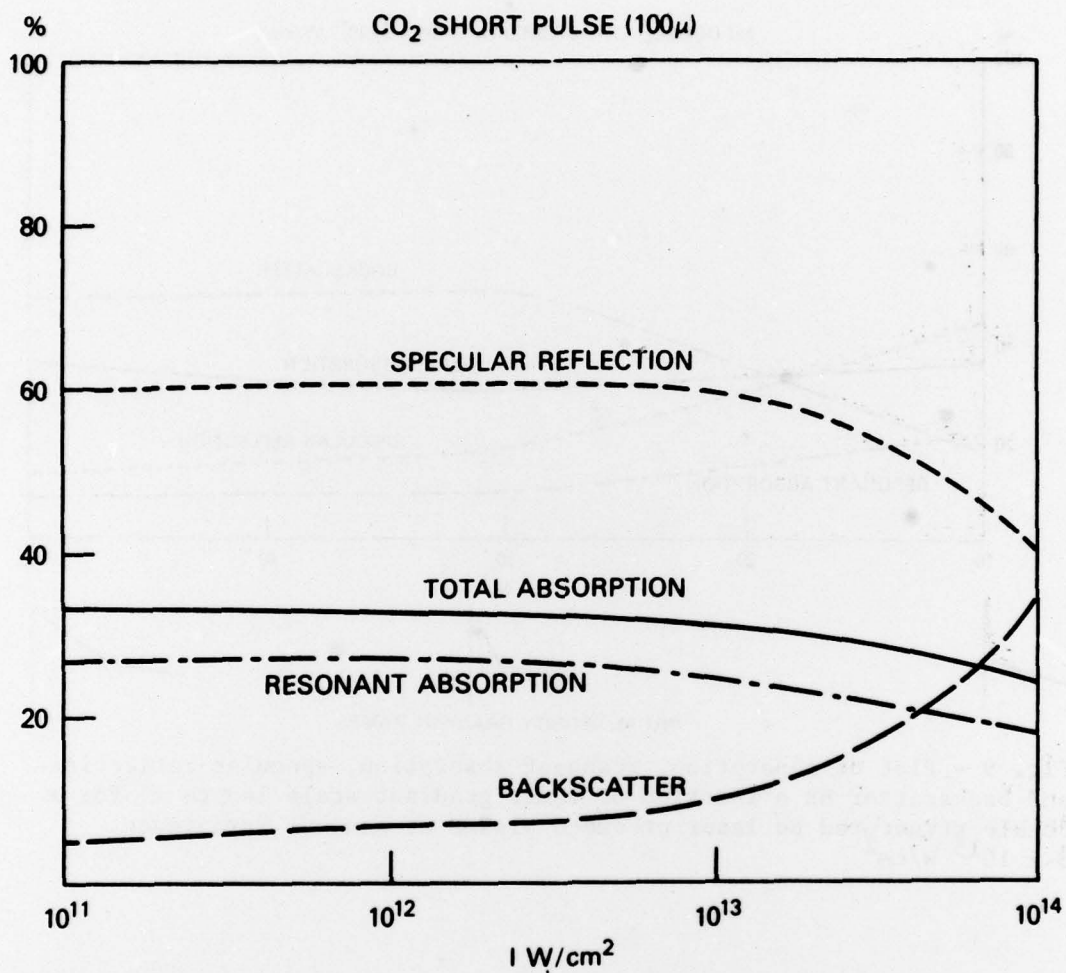

Fig. 7 - Plot of absorption, resonant absorption, specular reflection, and backscatter as a function of irradiance for a double structured pulse Nd laser plasma. The line which extends from 10^{15} - 10^{16} W/cm^2 is the NRL data

Nd DOUBLE-STRUCTURED (30-100μ)
SHORT PULSE

$T_{e\ max}$

V_{max}

$f(n = n_c)$

T_{keV}, f

$V_{cm/sec}$

10, 1

1, 10⁻¹

10⁻¹, 10⁻²

10⁸

10⁷

10⁶

10¹⁴   10¹⁵   10¹⁶   10¹⁷

I W/cm²
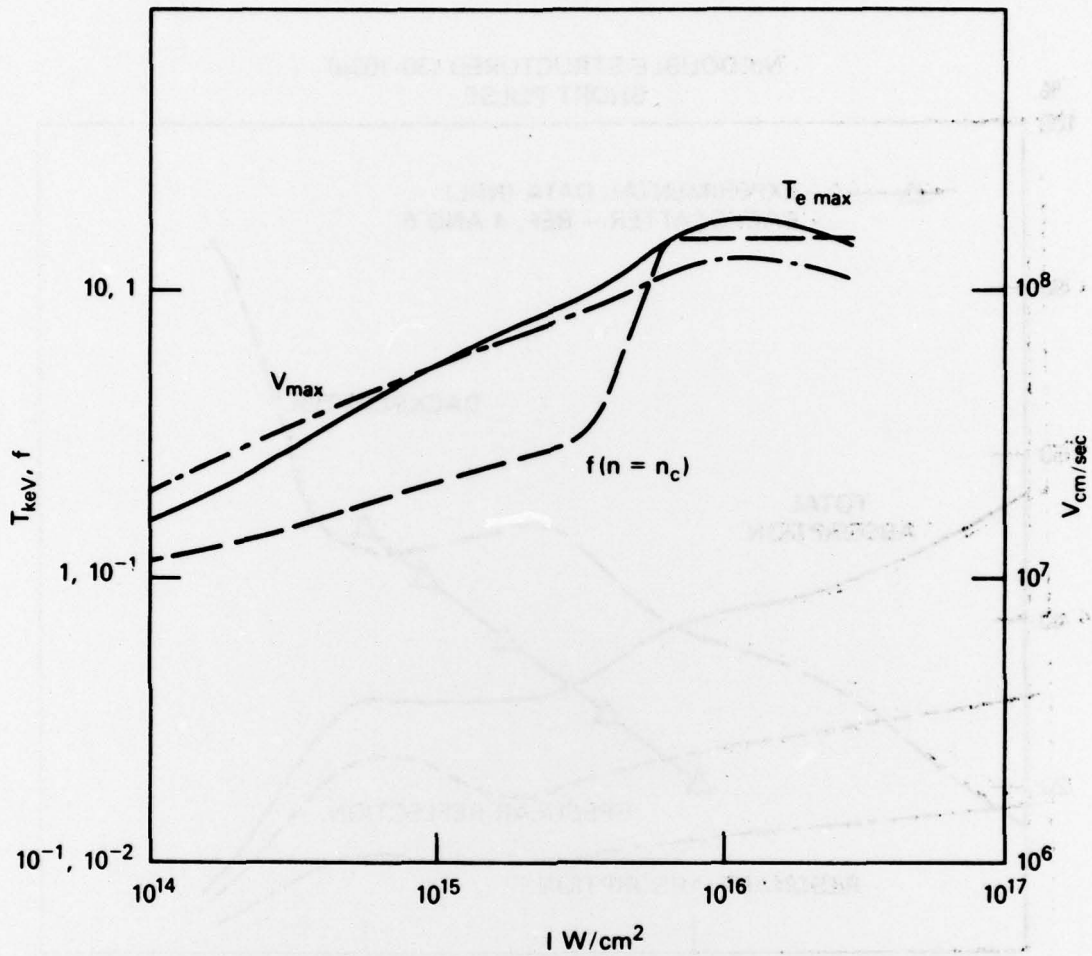
Fig. 8 - Plot of maximum electron temperature, ion blow-off velocity and flux limit as a function of irradiance for the plasma of Fig. 7

Fig. 9 - Plot of absorption, resonant absorption, specular reflection and backscatter as a function of inner gradient scale length x_μ for a double structured Nd laser produced plasma at maximum irradiance 3×10^{15} W/cm^2

59

Fig. 10 – Plot of absorption, resonant absorption, specular reflection and backscatter as a function of irradiance for a short pulse CO_2 laser produced plasma
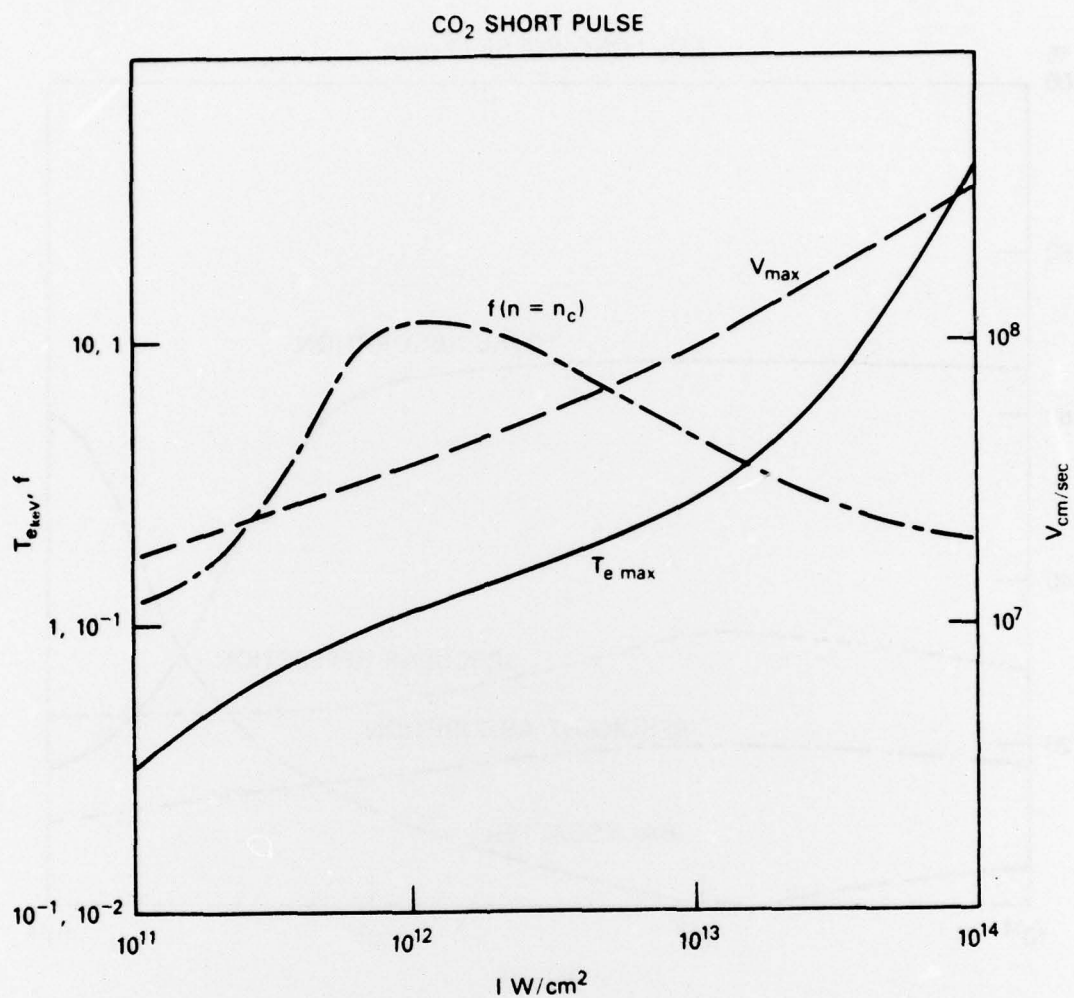
CO$_2$ SHORT PULSE

Fig. 11 - Plot of maximum electron temperature, ion blow-off velocity and flux limit at $n = n_c$ as a function of irradiance for the plasma of Fig. 10
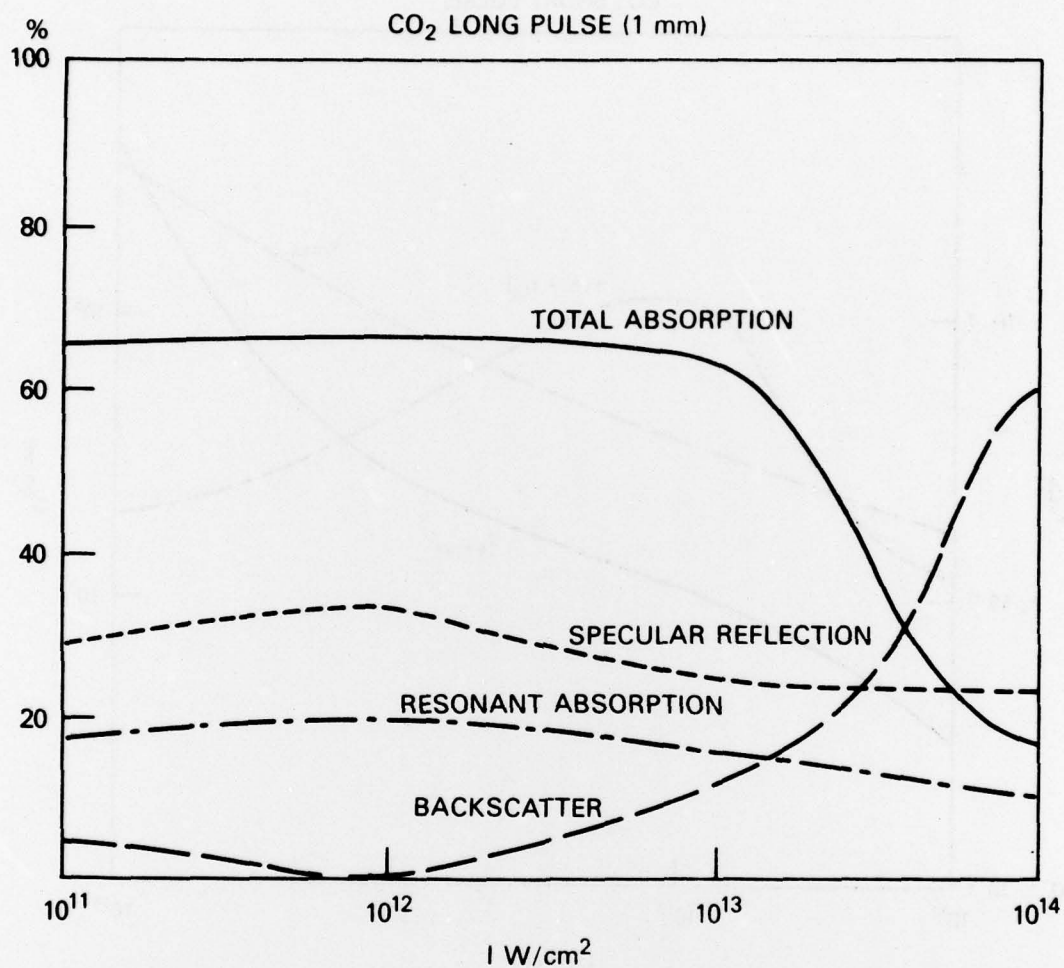
Fig. 12 - Plot of absorption, resonant absorption, specular reflection, and backscatter as a function of irradiance for a long pulse CO_2 laser produced plasma
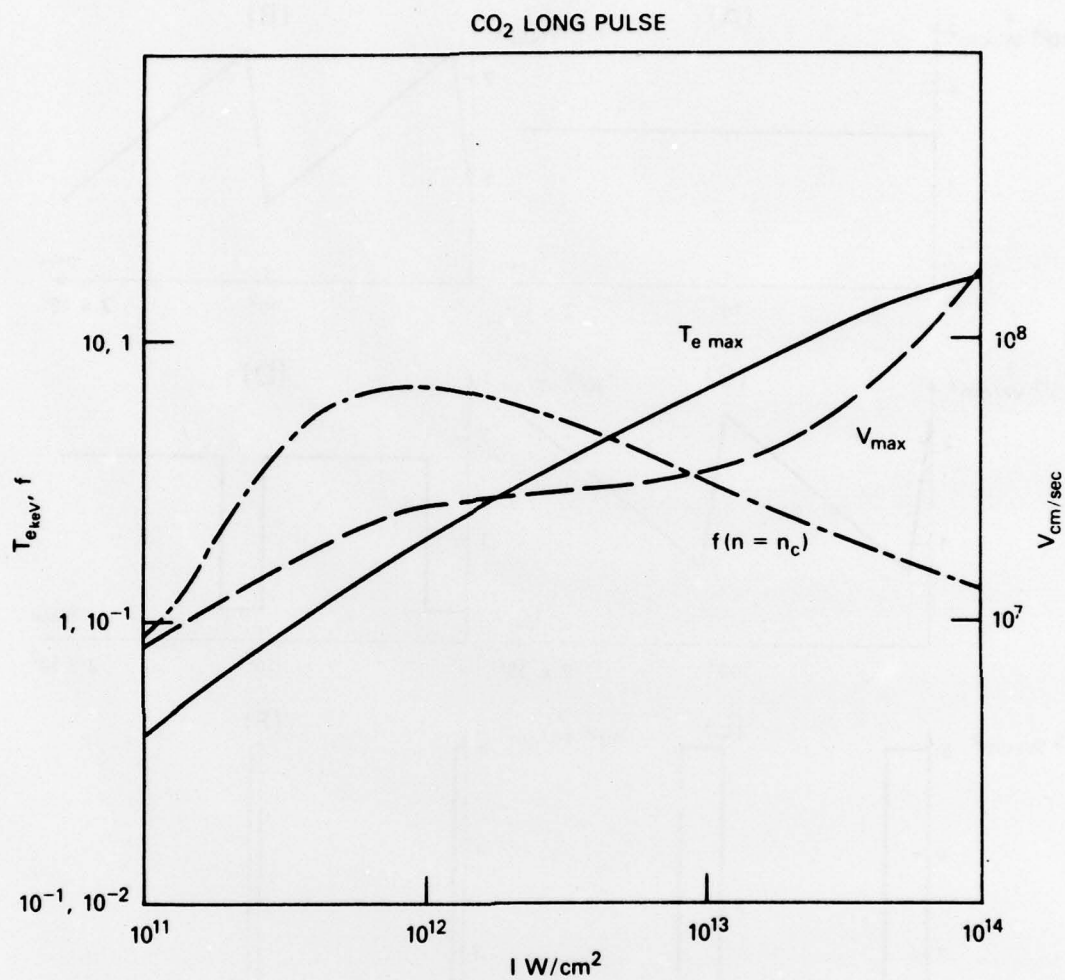
CO$_2$ LONG PULSE

Fig. 13 — Plot of maximum electron temperature, maximum ion blow-off velocity (i continues to accelerate for the duration of the simulation) and flux limit at n = n$_c$ as a function of irradiance for the plasma of Fig. 12
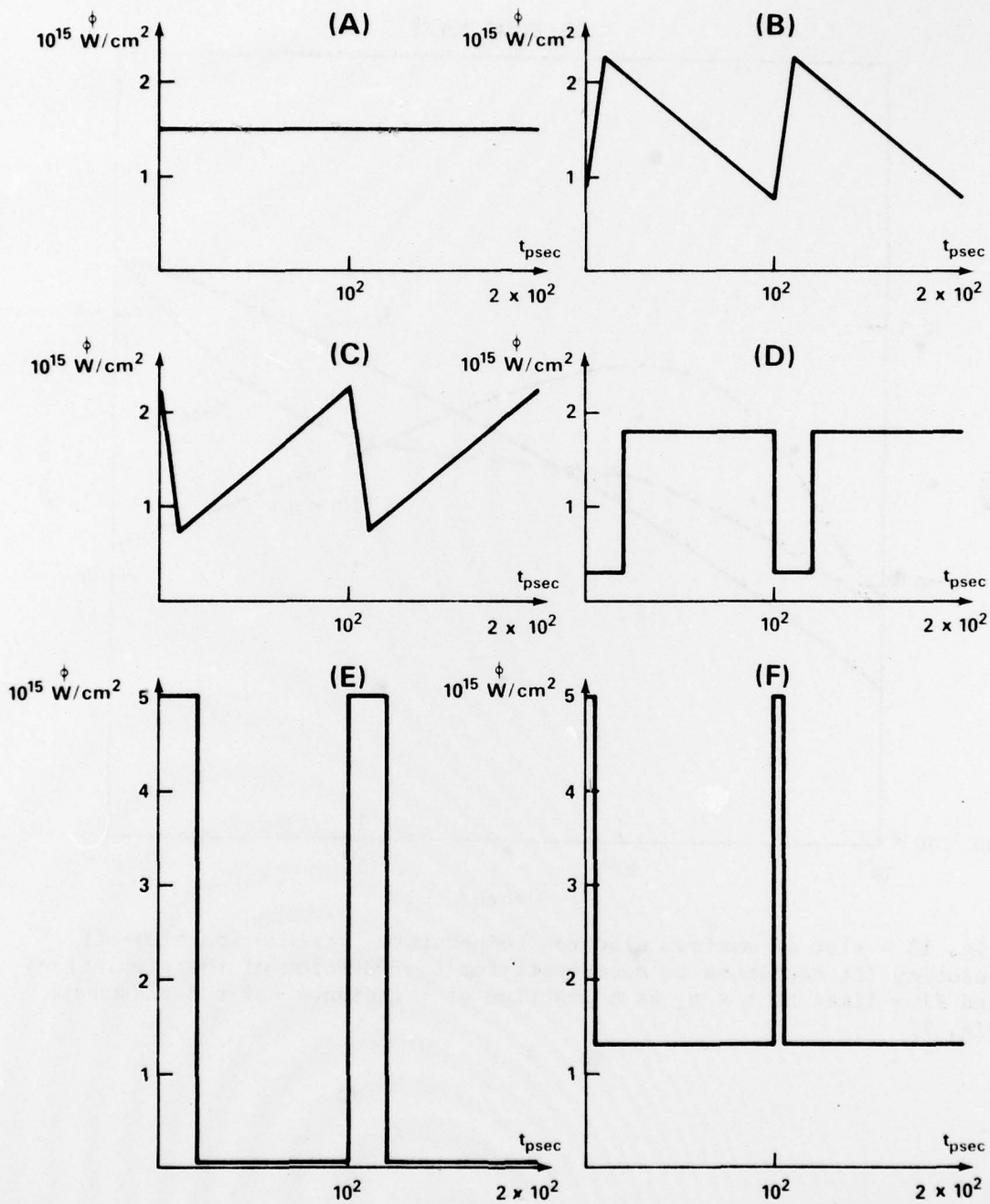
63

Fig. 14 - Picture of the temporal structure of the six pulse shapes simulated

64